The Astrophysical Journal, 902:94 (20pp), 2020 October 20 https://doi.org/10.3847/1538-4357/abb594

Shear-driven Transition to Isotropically Turbulent Solar Wind Outside the Alfvén Critical Zone

D. Ruffolo[1], W. H. Matthaeus[2], R. Chhiber[2,3], A. V. Usmanov[2,3], Y. Yang (杨艳)[4], R. Bandyopadhyay[5], T. N. Parashar[2,6], M. L. Goldstein[7], C. E. DeForest[8], M. Wan (万敏平)[4], A. Chasapis[9], B. A. Maruca[2], M. Velli[10], and J. C. Kasper[11,12]

[1] Department of Physics, Faculty of Science, Mahidol University, Bangkok 10400, Thailand; david.ruf@mahidol.ac.th
[2] Department of Physics and Astronomy and Bartol Research Institute, University of Delaware, Newark, DE 19716, USA
[3] Heliophysics Science Division, NASA Goddard Space Flight Center, Greenbelt, MD 20771, USA
[4] Department of Mechanics and Aerospace Engineering, Southern University of Science and Technology, Shenzhen, Guangdong 518055, People's Republic of China
[5] Department of Astrophysical Sciences, Princeton University, Princeton, NJ 08544, USA
[6] School of Chemical and Physical Sciences, Victoria University of Wellington, Wellington 6012, New Zealand
[7] Goddard Planetary Heliophysics Institute, University of Maryland Baltimore County, Baltimore, MD 21250, USA
[8] Southwest Research Institute, 1050 Walnut Street, Suite 300, Boulder, CO 80302, USA
[9] Laboratory for Atmospheric and Space Physics, University of Colorado Boulder, Boulder, CO 80303, USA
[10] Department of Earth, Planetary, and Space Sciences, University of California, Los Angeles, CA 90095, USA
[11] Climate and Space Sciences and Engineering, University of Michigan, Ann Arbor, MI 48109, USA
[12] Smithsonian Astrophysical Observatory, Cambridge, MA 02138, USA
Received 2020 July 28; revised 2020 September 1; accepted 2020 September 3; published 2020 October 15

Abstract

Motivated by prior remote observations of a transition from striated solar coronal structures to more isotropic "flocculated" fluctuations, we propose that the dynamics of the inner solar wind just outside the Alfvén critical zone, and in the vicinity of the first $\beta = 1$ surface, is powered by the relative velocities of adjacent coronal magnetic flux tubes. We suggest that large-amplitude flow contrasts are magnetically constrained at lower altitude but shear-driven dynamics are triggered as such constraints are released above the Alfvén critical zone, as suggested by global magnetohydrodynamic (MHD) simulations that include self-consistent turbulence transport. We argue that this dynamical evolution accounts for features observed by Parker Solar Probe (PSP) near initial perihelia, including magnetic "switchbacks," and large transverse velocities that are partially corotational and saturate near the local Alfvén speed. Large-scale magnetic increments are more longitudinal than latitudinal, a state unlikely to originate in or below the lower corona. We attribute this to preferentially longitudinal velocity shear from varying degrees of corotation. Supporting evidence includes comparison with a high Mach number three-dimensional compressible MHD simulation of nonlinear shear-driven turbulence, reproducing several observed diagnostics, including characteristic distributions of fluctuations that are qualitatively similar to PSP observations near the first perihelion. The concurrence of evidence from remote sensing observations, in situ measurements, and both global and local simulations supports the idea that the dynamics just above the Alfvén critical zone boost low-frequency plasma turbulence to the level routinely observed throughout the explored solar system.

Unified Astronomy Thesaurus concepts: Solar wind (1534); Interplanetary turbulence (830); Space plasmas (1544); Interplanetary magnetic fields (824)

1. Introduction

The solar atmosphere originates in the highly dynamic photosphere and expands outward, generating the magnetically dominated corona. The outward acceleration eventually causes the velocity to exceed the local Alfvén speed, and in that super-Alfvénic regime, embedded magnetic fluctuations will only propagate outward. Consequently, a feature distinguishing the inner corona from the super-Alfvénic solar wind is that magnetohydrodynamic (MHD) fluctuations can propagate both upward and downward in the inner corona but, in the solar wind, such signals cannot propagate back into the corona. The hypothetical boundaries between these regions are the Alfvén critical surface, where the Alfvén speed of magnetic fluctuations equals the solar wind speed, and the sonic critical surface, where the speed of sound equals the solar wind speed. In view of the highly dynamic, or turbulent, nature of both the solar wind and corona, these boundaries are almost certainly better described as critical *zones* (DeForest et al. 2018). For many years, there has been discussion and speculation regarding what happens near and at these zones. In the simplest picture (the surface version), Alfvén or sound waves can propagate only outward at the surface. Downward propagating fluctuations below the Alfvén surface cannot reach the solar wind. Downward propagating fluctuations above the Alfvén critical zone in the solar wind cannot propagate back into the sub-Alfvénic corona. It would not be unreasonable to imagine that, with such stagnation of downward-moving fluctuations and their interaction with upward-moving fluctuations, turbulence levels build up in the critical zone, a possibility that has also been suggested based on remote sensing observations (Lotova et al. 1985, 2011). This reasoning has also long been offered as explaining why the inner solar wind is dominated by a broadband spectrum of *outward traveling* waves (Belcher & Davis 1971). This "Alfvénic" property of the fluctuations is characteristic of the inner heliosphere, where it forms a power-law inertial range observed from the correlation scale to the ion inertial scale (Bavassano et al. 1982; Bruno & Carbone 2013). The corona is presumed to be turbulent and the solar wind is observed to be turbulent from the distance of the latest Parker Solar Probe (PSP; Fox et al. 2016) perihelia measurements out

to the boundary of the heliosphere beyond 100 au. But how this turbulence changes in character across the critical zones is not well understood. Furthermore, the nature of the transitions in all plasma properties from coronal to solar wind conditions remains to be discovered. Fortunately, PSP data are revealing these properties at progressively lower altitudes, and more information will soon be forthcoming from the recently launched Solar Orbiter (Müller et al. 2013) mission. Together, these two missions are expected to unravel many mysteries of the inner solar wind and outer corona, including the issues we investigate here.

Initial results from PSP have revealed magnetic reversals and velocity spikes (Bale et al. 2019; Kasper et al. 2019; Dudok de Wit et al. 2020) similar to previous observations at 0.3 au and beyond (Michel 1967; Kahler et al. 1996; Balogh et al. 1999; Crooker et al. 2004; Borovsky 2016; Horbury et al. 2018; Lockwood et al. 2019). One explanation is that the reversals arise from outward propagation of large-amplitude remnants of magnetic reconnection that occurred at lower altitudes (Axford & McKenzie 1992; Axford et al. 1999; Samanta et al. 2019; Fisk & Kasper 2020). Such a mechanism is plausible and difficult to rule out. However, another possibility is that the reversals reflect an onset of strong shear-driven turbulence that began just outside the Alfvén critical zone where the solar wind speed first exceeded the Alfvén speed. Such shears could produce magnetic reversals through large-scale perturbations of the flow. For example, such perturbations could result from excitation of the Kelvin–Helmholtz instability (Malagoli et al. 1996).

This scenario is consistent with a suite of observable effects already apparent in imaging (DeForest et al. 2016) and in situ data sets (Borovsky 2016; Horbury et al. 2018). In particular, DeForest et al. (2016) interpreted the transition from elongated striae to relatively isotropic flocculae as a signature of the onset of shear-driven turbulent activity some 20–80 solar radii from the photosphere, where the magnetic field ceases to be a dominant constraint on transverse motions. In the present work, following DeForest et al. (2016), we refer to this process as flocculation. This interpretation is supported by results from turbulence-driven global simulations of the solar wind (Chhiber et al. 2018). The presence of velocity shears is also strongly suggested by coronal imaging at lower altitudes (DeForest et al. 2018).

Here we use PSP observations in its first two orbits, along with supporting simulations, to examine the character of the plasma dynamics in the solar wind at heliocentric distance r as low as 36 $R_\odot$ (0.17 au), along with evidence that PSP approached the Alfvén critical zone. Our presentation incorporates global heliospheric MHD simulations, local three-dimensional (3D) compressible MHD simulation, and PSP observations. The goals are to understand the region where flocculation is believed to start, to identify signatures of the process of flocculation in PSP data, and to evaluate the hypothesis that the transition from striation to flocculation is a consequence of velocity shears. We are therefore led to consider physics related to nonlinear shear instabilities, essentially nonlinear Kelvin–Helmholtz dynamics or mixing-layer dynamics, appropriately generalized to an MHD or plasma environment. While we cannot definitively resolve these questions based on the current observational evidence, global simulation, and supporting simulation of local physics, we nonetheless are able to conclude that the available evidence is consistent with our hypothesis of the role of velocity shear in the inner solar wind.

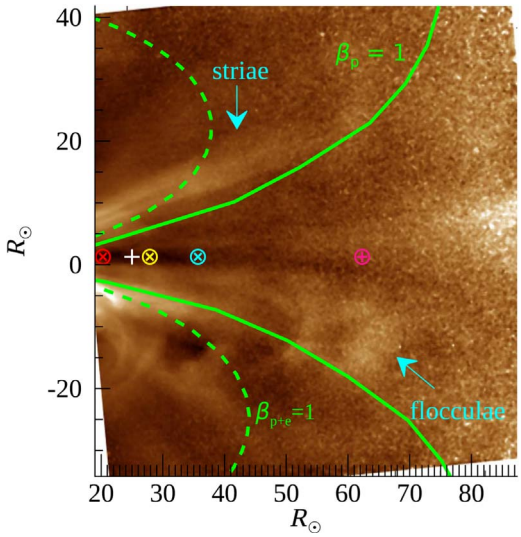

Figure 1. STEREO Heliospheric Imager snapshot from 2008 December 16, analyzed as in DeForest et al. (2016) and Chhiber et al. (2018), showing the transition with radial evolution from a highly anisotropic striated conformation closer to the Sun, to a more isotropic flocculated conformation at greater distances. Also indicated are first $\beta = 1$ surfaces (green curves) from a global heliospheric MHD simulation, based on a magnetogram corresponding to 2008 December. For this simulation, the Alfvén surface lies below 15 $R_\odot$ (see Chhiber et al. 2018). From right to left, circled symbols indicate the Helios perihelion (⊕) and the first, fourth, and sixth PSP perihelia (⊗). The white plus sign shows the location of enhanced turbulence inferred by Lotova et al. (1985). In the present paper, we develop the hypothesis that this transition is fueled by nonlinear shear instability outside the Alfvén critical zone.

2. Motivation and Hypothesis

2.1. Heliospheric Imaging from STEREO

DeForest et al. (2016) analyzed image sequences recorded by the inner Heliospheric Imager instrument on board the Solar-Terrestrial Relations Observatory (STEREO/HI1) in 2008 December. The analysis covered angular distances of approximately 4° to 24° from the center of the Sun. An observed systematic transition in the images was noted that consisted of anomalous fading of the radial striae that characterize the corona, along with an anomalous relative brightening of locally dense puffs of solar wind, which were described as "flocculae." This transition was interpreted as the onset of dynamical activity associated with velocity shear present in the nascent solar wind plasma coming from near-radial corotating flux tubes in the corona. The flux tubes confine the plasma, magnetic structures, and fluctuations that were injected at lower altitudes. Moving radially outward, the magnetic field progressively loses control of the plasma, which allows for additional physical processes to dominate, including those that give rise to the striation-flocculation transition. Significant stages of this transition are indicated by passage through regions where the flow speed exceeds the Alfvén speed (the Alfvén critical zone) and where the mechanical pressure approaches or exceeds the magnetic pressure (first $\beta = 1$ zones).

Figure 1 illustrates a frame of the DeForest et al. (2016) analysis, in which the transition from striation to flocculation is

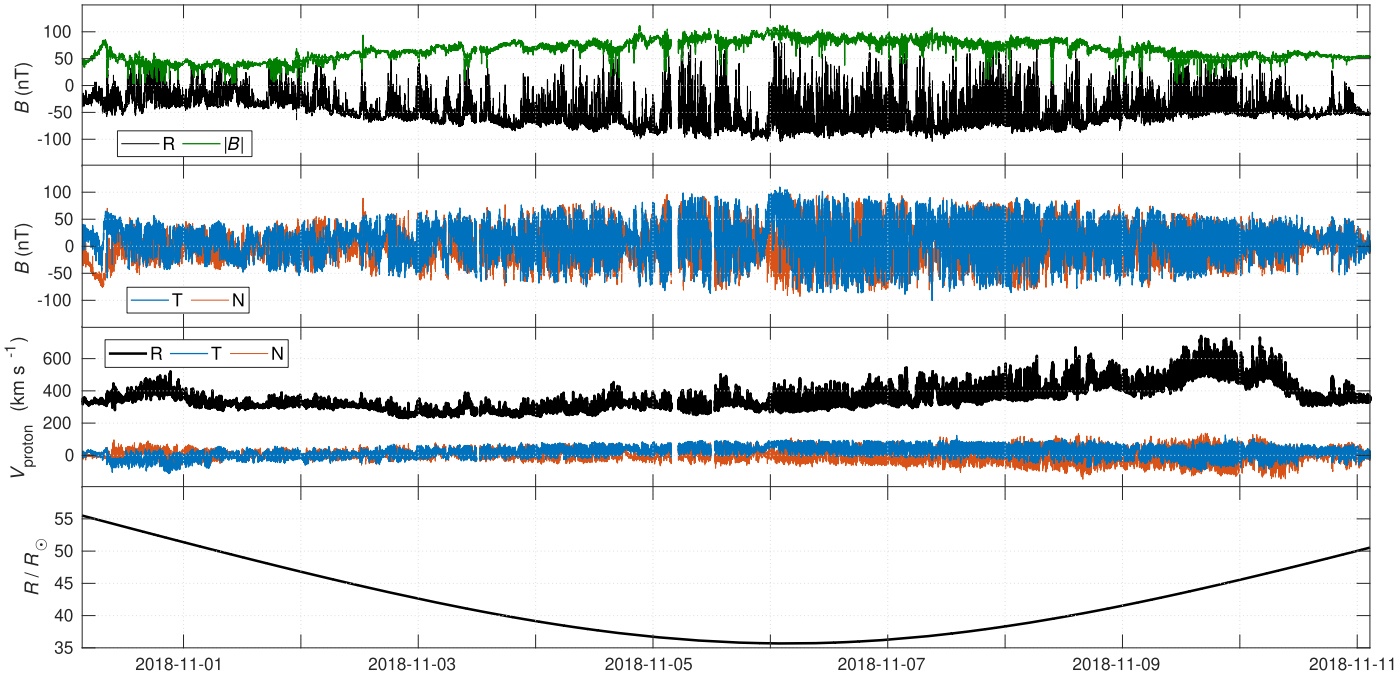

Figure 2. Overview of part of the first PSP encounter. Top panel: Radial component (black) and magnitude (red) of the magnetic field; occurrence of numerous switchbacks (radial component reversals) is evident, although the magnitude exhibits much less variation. Second panel: Tangential (blue) and normal (red) components of the magnetic field. Third panel: Proton velocity components, with the same colors. The data plotted in (a)–(c) all have a cadence of 1 NYs $\approx$ 0.87 s. Bottom panel: Radial distance of PSP from the center of the Sun in units of solar radii.

clear. The tendency for the structures in the image to become more isotropic with increasing heliocentric distance was quantified by DeForest et al. (2016) by computations of radial and transverse-to-radial second-order structure functions of the signal. Closer to the Sun, the striation is due to more intense gradients in the transverse direction and weaker radial gradients, indicated by values of transverse structure functions greater than radial structure functions at a given lag. Moving outward, the corresponding values of the two structure functions become more equal, indicating an evolution toward isotropy.

Figure 1 is also annotated with approximate equivalent positions of the first, fourth, and sixth PSP perihelia, and the perihelion of the Helios mission at 0.29 au. Based on global MHD simulations that include turbulence transport (Chhiber et al. 2019a), the figure also shows the first surfaces where the plasma beta is unity when considering protons and electrons ($\beta_{p+e} = 1$) and when considering only protons ($\beta_p = 1$). For the simulation considered here, the Alfvén surface lies below 15 $R_\odot$, to the left of the view in this image.

2.2. Parker Solar Probe: Review of Prior Results

During its first few orbits, the PSP mission has made pioneering observations in the inner solar wind that bear directly on the questions we explore here. PSP is currently in its sixth orbit and may be approaching the Alfvén critical zone, and will thus be directly examining the region of interest. We will delve into the observations in more detail below, but to begin the discussion, Figure 2 illustrates some of the important and relevant measurements made by PSP from 2018 October 31 to November 11, an 11 day period surrounding its first perihelion at 35.7 solar radii (0.17 au) on 2018 November 6 at 0327 UT. Cartesian components of magnetic and velocity fields and the density are shown for this period at a cadence of 1 "New York second" (NYs) $\approx$ 0.87 s, the fundamental cadence of solar wind velocity measurements. These data will be discussed in greater detail below, and our hypothesis will be evaluated in terms of a number of details of these observations. For the moment, we wish to call attention to a particular feature that has been written about in a number of the early PSP publications (Bale et al. 2019; Kasper et al. 2019; Mozer et al. 2020; Dudok de Wit et al. 2020), *viz.*, the phenomenon of *switchbacks*, which has particular relevance to our proposed model. PSP observations during most time periods near the first and second perihelia indicated a mean magnetic field that was nearly radially inward. However, the data frequently indicate weakening and sometimes reversals (i.e., switchbacks) in the radial magnetic field B_R. The weakening is accompanied by the appearance of substantial transverse components, i.e., T and N components in the standard spacecraft-centered orthogonal RTN coordinate system, where +R is radial (antisunward), +T is tangential (toward increasing heliolongitude), and +N is normal (toward increasing heliolatitude). Note that vector velocities in this frame are measured relative to the fixed stars, that is, the spacecraft velocity has been subtracted out of the solar wind velocity measurement.[13] These features are apparent in the corresponding panels of Figure 2 and are discussed further below.

In what follows, we will argue that switchbacks and related features of the complex dynamics observed by PSP in this region can be explained by in situ shear-driven dynamics and are also consistent with the striation-flocculation transition described in DeForest et al. (2016). Previous arguments in favor of an in situ origin of switchbacks and large-amplitude magnetic fluctuations were made by Squire et al. (2020), based on expanding-box compressible MHD simulations, and Macneil et al. (2020), based on Helios observations of

[13] See the SWEAP Data User's Guide.

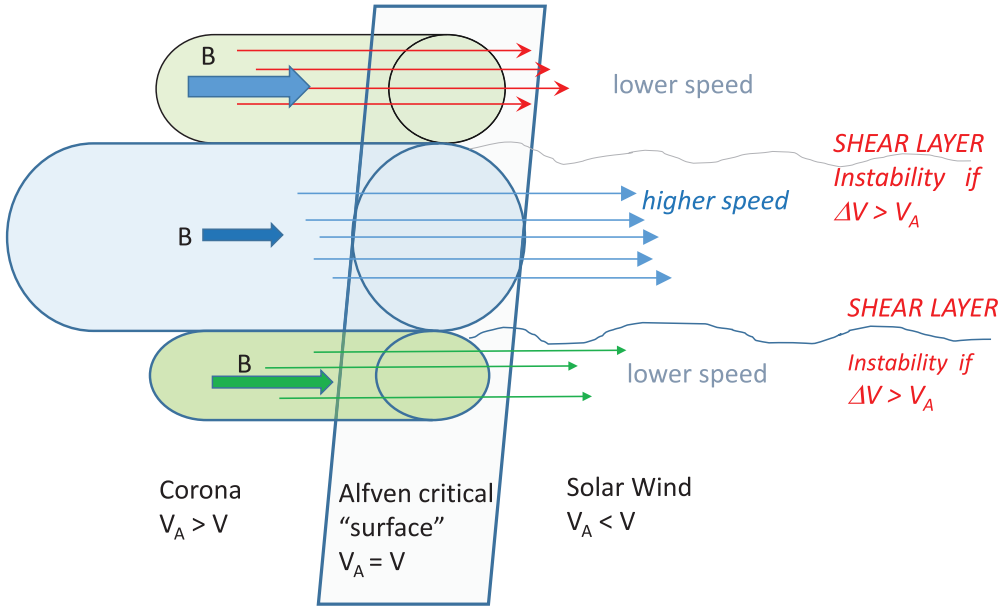

Figure 3. Sketch describing our proposed hypothesis. In the corona, the strong magnetic field regulates the dynamics of the nascent solar wind. Each flux tube may contain differing radial speeds and different radial field strengths due to processes at lower altitudes. Beyond the Alfvén critical zone, the magnetic field is no longer capable of constraining the dynamics and the energy in the velocity contrasts becomes available to drive nonlinear magnetized Kelvin–Helmholtz-like dynamics, including magnetic field amplification and directional change, with associated deflection of velocities into the transverse directions. This may explain the transition from striation to flocculation in STEREO images such as that in Figure 1 and, in the present work, we point out characteristics of PSP data that are consistent with this picture of how shear-driven dynamics at and above the Alfvén critical zone boosts low-frequency turbulence to the levels observed throughout the heliosphere.

switchbacks, which were more frequent at greater distance from the Sun.

2.3. Hypothesis of Shear-driving: Cartoon

Our initial hypothesis is an extrapolation of the ideas in DeForest et al. (2016), in which the morphological transition between striation and flocculation that is apparent in the STEREO images reflects a transition from largely collimated elongated structures, relatively slowly varying in radius, to more disordered shapes suggestive of a more isotropic distribution of fluctuations. This was attributed to an isotropization of turbulence as the magnetic field above the Alfvén critical zone (and later above a first $\beta = 1$ zone) gives up much of the control over the plasma that it maintained in the highly magnetized sub-Alfvénic corona.

Here we pursue a particular form of that hypothesis, in which above the Alfvén critical surface or zone, the velocity differences between adjacent flux tubes may be tapped to supply energy for a more isotropic form of turbulence. The physical picture we have in mind involves essentially nonlinear magnetized Kelvin–Helmholtz dynamics, perhaps better described as a magnetized mixing layer. A highly simplified sketch of the scenario we propose is provided in Figure 3.

2.4. Hypothesis of Shear-driving: Expectations and Background

In examining whether shear-driven dynamics are responsible for prominent features observed by PSP near perihelion, we are led to consider basic physics suggested in Figure 3 that is similar to the classic hydrodynamic problem of a mixing layer (Rogers & Moser 1992). When two colinear streams having different velocities come into contact, the early part of the dynamics can resemble a linear Kelvin–Helmholtz instability, quickly evolving into a nonlinear mixing layer characterized by vortex rollup.

The addition of a uniform parallel magnetic field into the problem presents the complication that the transverse displacements needed to produce rollup are inhibited by magnetic field line tension. The linear theory of stability of planar MHD shear layers, a magnetized Kelvin–Helmholtz instability, was considered by Chandrasekhar (1981), who stated the important condition that the instability is suppressed when the velocity contrast does not exceed the Alfvén speed, that is when $\Delta V < V_A$. This instability was subsequently considered in greater detail by Lau & Liu (1980) and Miura & Pritchett (1982) who refined instability criteria for particular assumptions. More generally, one does not expect that the mixing-layer dynamics will be described by linear theory, particularly in cases in which the initial state is not an equilibrium and turbulence, possibly broadband, is present within the velocity streams.

To examine the nonlinear evolution of MHD mixing-layer/Kelvin–Helmholtz dynamics, Miura (1982) appealed to numerical simulation of compressible MHD. In the nonlinear regime, rollup of both vortices and magnetic field occurs with a substantial component of transient amplification of magnetic energy. Similar configurations were investigated using an incompressible MHD model (Goldstein et al. 1987, 1989) with the goal of understanding magnetospheric boundary effects and reduction of cross-helicity (Alfvénicity) in the solar wind (Roberts et al. 1992). Further study using a compressible model (Malagoli et al. 1996) revealed additional details of the rollup process, which involves strong coupling between flows and magnetic field structure. In particular, for cases in which the magnetic field is not strong enough to stabilize the dynamics, the fully developed state is substantially influenced

by the presence of the (amplified) magnetic field, which exhibits distinctive structure within the vortex roll-ups.

We should note that related studies (Dahlburg et al. 1998; Einaudi et al. 1999) employed an incompressible MHD model to examine the linear and nonlinear evolution of a radial jet confined within a neutral sheet. This system, in effect a simplified model of a coronal streamer, also exhibits Kelvin–Helmholtz-like dynamics at distances large enough that the jet speed exceeds a multiple of the Alfvén speed. Instability and topological changes in the magnetic field at the tip of such a streamer were considered in Rappazzo et al. (2005). The effect of shear and expansion on a spectrum of Alfvénic fluctuations, previously examined by incompressible simulation (Roberts et al. 1992) and in turbulence transport theory (Breech et al. 2008), was recently considered using expanding-box simulation in the context of PSP data in Shi et al. (2020).

Below we will examine our hypothesis by comparison of features of PSP observations near perihelion to computed features of 3D compressible MHD mixing-layer simulations. We note that similar comparisons were employed to explain polarity reversals seen in data from the *Ulysses* spacecraft (Landi et al. 2005, 2006).

3. Methods

3.1. Observations by the Parker Solar Probe

In the present paper, we make use of publicly available data from the first two orbits of PSP, from two instrument suites, FIELDS (Bale et al. 2016) and SWEAP (Kasper et al. 2016).[14] We use Level 2 magnetic field data from FIELDS, which typically have a data rate of 299 Hz, and Level 3 plasma data from SWEAP, with solar wind speed typically available at a cadence of 1 NYs. We then usually resample both types of data to either 1 NYs or 1 s cadence, and plasma data from SWEAP are processed to remove spurious spikes. The latter procedure makes use of a time-domain Hampel filter (Davies & Gather 1993), with a filtering interval of 120 s and outliers identified as values more than three times larger than the local standard deviation. We designate the inner segments of these orbits (about two months surrounding perihelion) as the first (solar) encounter (E1), roughly during 2018 October–November, and the second encounter (E2), roughly during 2019 March–April. Observations during E1 were well described in the first results papers (Bale et al. 2019; Kasper et al. 2019) and in relevant papers in the special Astrophysical Journal Supplement issue (e.g., Dudok de Wit et al. 2020; Mozer et al. 2020).

3.2. Global Solar Wind Simulations

We employ global 3D MHD modeling to compare with several features of PSP observations that will be discussed in following sections. The fully 3D model that we employ is based on mean-field (Reynolds-averaged) solar wind equations, which are solved simultaneously with turbulence transport equations (Usmanov et al. 2018). The equations also include electron heat conduction, Coulomb collisions, Reynolds stresses, and electron/proton heating by a turbulent cascade. The resolved equations and unresolved (subgrid-scale) turbulence equations are solved self-consistently.[15] The turbulence model includes three equations: for turbulence energy, normalized cross-helicity, and correlation length.

The current computation has evolved from previous work (Usmanov et al. 2014, 2016, 2018) and is carried out in four regions: (1) corona, 1–20 $R_\odot$, (2) inner heliosphere, 20 $R_\odot$ −5 au, (3) middle heliosphere, 5–40 au, and (4) outer heliosphere, 40–1200 au. Boundary conditions are specified at the coronal base (just above the transition region) using ADAPT (Air Force Data Assimilative Photospheric Flux Transport) solar synoptic magnetic field maps (Arge et al. 2010; Hickmann et al. 2015), in which flux evolution models for the photospheric magnetic field are assimilated with photospheric magnetic field observations. We use the ADAPT map, which is based on the GONG (Global Oscillation Network Group) magnetogram, with the central meridian time 2018 November 6 at 12:00 UTC. The ADAPT map values are scaled by a factor of 2 and are smoothed using a spherical harmonic decomposition up to 15th order.

This global solar wind simulation model has been under continual development (Usmanov et al. 2018) and was recently employed to provide context for the STEREO observations described in Section 2.1 and also to generate contextual predictions for the PSP mission (Chhiber et al. 2019a, 2019b).

3.3. Compressible MHD Simulations of Mixing-layer Dynamics

To demonstrate the basic physics associated with our hypothesis, we have carried out a series of nonlinear simulations of fluid-scale turbulence triggered by strong velocity shear in the presence of a moderately strong uniform DC magnetic field. We solve the compressible MHD equations via a hybrid compact-weighted essentially non-oscillatory (WENO) scheme, which couples a sixth-order compact scheme for smooth regions and a fifth-order WENO scheme for shock regions. The time marching is performed by the third-order Runge–Kutta scheme.

The numerical simulations are conducted either in two dimensions (2D) in a $(2\pi)^2$ domain with 256^2 resolution, or in three dimensions (3D) in a $(2\pi)^3$ domain with 256^3 resolution, all with periodic boundary conditions. For simplicity, equal viscosity and resistivity are used, i.e., the magnetic Prandtl number is set equal to unity and an ideal gas equation of state is adopted. While we have varied some initial parameters to investigate the robustness of our conclusions, here we report results from one representative 3D simulation. Initially flow reversal occurred across two thin layers at $y = L_y/4$ and $y = 3L_y/4$, where $L_y = 2\pi$. Initially the velocity and magnetic field are only in the x-direction. The x-direction velocity is given by

$$u_x = U_0 \left[1 - \tanh\left(\frac{y - L_y/4}{d}\right) + \tanh\left(\frac{y - 3L_y/4}{d}\right)\right], \quad (1)$$

[14] All data were downloaded from https://cdaweb.gsfc.nasa.gov/pub/data/psp/.

[15] We use Reynolds averaging based on an ensemble average $\langle ... \rangle$ (McComb 1990). One decomposes a variable, such as the velocity $\boldsymbol{u}$, as $\boldsymbol{u} = \langle \boldsymbol{u} \rangle + \boldsymbol{u}'$ where $\langle \boldsymbol{u} \rangle$ is the mean and $\boldsymbol{u}'$ is the unresolved or fluctuating component. Reynolds averaging of nonlinear terms involves contributions from fluctuations such as $\langle u_i' u_j' \rangle$, known as the Reynolds stress, which is particularly prominent when fluctuations are incompressible.

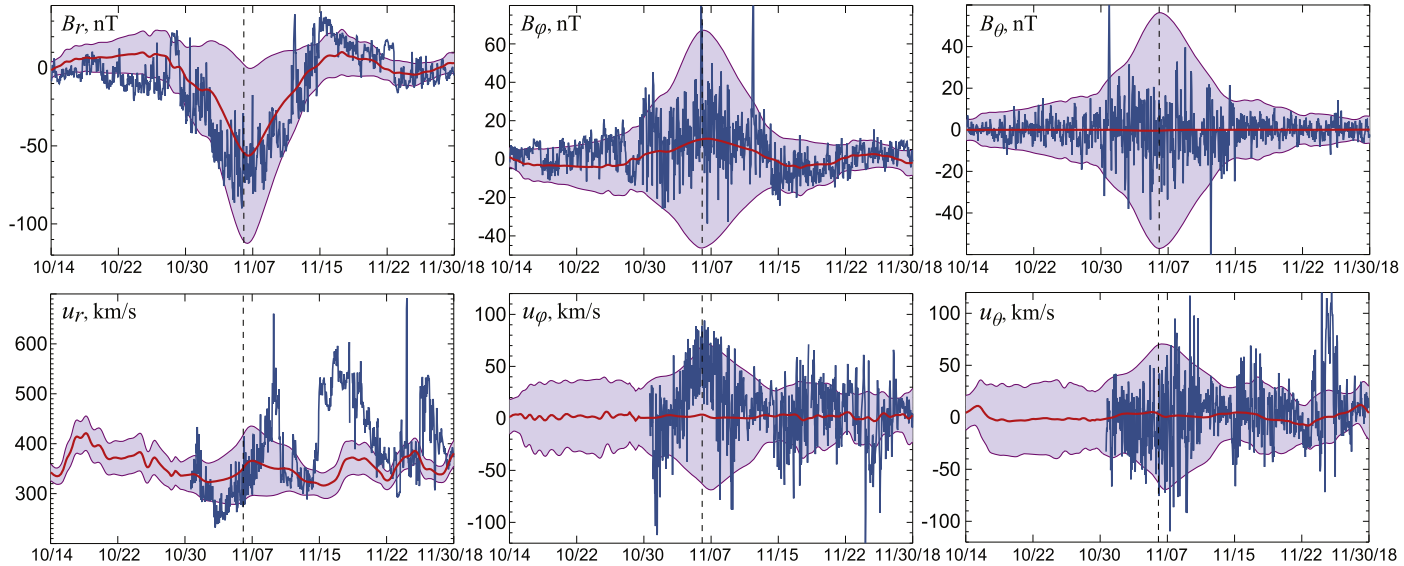

Figure 4. Magnetic field (top) and velocity (bottom) components (left: radial, center: azimuthal, right: meridional) measured by PSP during the first encounter, shown as hour averages (blue line). Also shown are resolved (mean field) solutions for the corresponding magnetic field components from the Usmanov et al. (2018) global simulation employing an ADAPT magnetogram corresponding to the period of the encounter. Finally the shaded background is an envelope corresponding to an estimate of the turbulence amplitude relative to the mean field computed in the simulation using self-consistent turbulence transport equations as explained in the text.

Table 1
Initial Parameters for Shear-driven 3D Compressible MHD Simulation by Methods of Yang et al. (2016)

$\Delta U/V_A$	3.0
Plasma β	1
Mach number M_t	3.6
Flow speeds u_x	± 0.27
B_x (strong region)	0.18
B_x (weak region)	0.08
Code resolution	256^3

where $U_0 = 0.27$ and $d = 0.025L_y$ is one-half the thickness of the shear layer. Similarly, the x-direction magnetic field is given by

$$B_x = C_1\left[1 - \tanh\left(\frac{y - L_y/4}{d}\right) + \tanh\left(\frac{y - 3L_y/4}{d}\right)\right] + C_2, \quad (2)$$

where $C_1 = 0.05$ and $C_2 = 0.13$ in our simulation. Therefore, the velocity streams have $u_x = +U_0$ or $u_x = -U_0$, while the magnetic field in the same stream regions has $B_x = C_1 + C_2 = 0.18$ or $B_x = C_2 - C_1 = 0.08$, respectively, in Alfvén speed units. The magnetic field is initially entirely toward $+x$, stronger in the top and bottom regions and weaker in the middle region. In this arrangement, qualitatively consistent with the diagram in Figure 3, the current layers between flux tubes are collocated with the vorticity layers separating streams.

Some of the parameters of the representative 3D simulation are shown in Table 1. The simulation initially has uniform density $\rho = 1$ and a velocity difference between streams of $\Delta U/V_A = 2U_0/V_A = 3$, where V_A is derived from the strong field region. The plasma beta, i.e., the ratio of plasma pressure to magnetic field pressure, is $\beta = 1$. The initial turbulent Mach number is $M_t = \Delta U/c_s = 3.6$ for sound speed c_s. The initial temperature pattern is set to achieve uniform total pressure. The value of the polytropic index is $\gamma = 1.4$, a value for which extensive testing of the code was carried out for high Mach number MHD turbulence as described by Yang et al. (2016). Details of the implementation, transport coefficients, and other numerical details are given in the same reference.

4. Results: Parker Solar Probe Observations

4.1. Expectation of High Turbulence Levels Near the Alfvén Critical Zone

Global simulations of the same type as those described in Section 3.2 predict (Chhiber et al. 2019a) a high level of turbulence in the neighborhood around and near the Alfvén critical surface (or zone). Physically, this relates to outward traveling Alfvénic fluctuations and the stagnation of inward fluctuations as described earlier. To some degree, this may also be anticipated by simpler, non-self-consistent treatments such as WKB theory (Hollweg 1974), turbulence transport theory (Zank et al. 1996) and, more recently, expanding-box simulations (Squire et al. 2020). From the self-consistent simulations, the predicted value of the ratio of magnetic fluctuation intensity to the strength of the resolved magnetic field, $\delta B/B_0$, is expected to be near unity or even above in this zone (Chhiber et al. 2019b). This is the same region in which remote radio observations have found enhanced scattering, from which enhanced turbulence levels are inferred (Lotova et al. 2011).

Further evidence is presented by new global simulation results shown in Figure 4 that address more specifically the likelihood of large polarity reversing magnetic fluctuations. Such simulations provide valuable insights into the behavior of the solar wind velocity and magnetic field components along the first three PSP orbits.

At the cadences shown in Figure 4, neither the observations nor the simulations capture the full fluctuation amplitudes (which can be seen in Figure 2). The global code includes a self-consistent transport model for the turbulence amplitude,

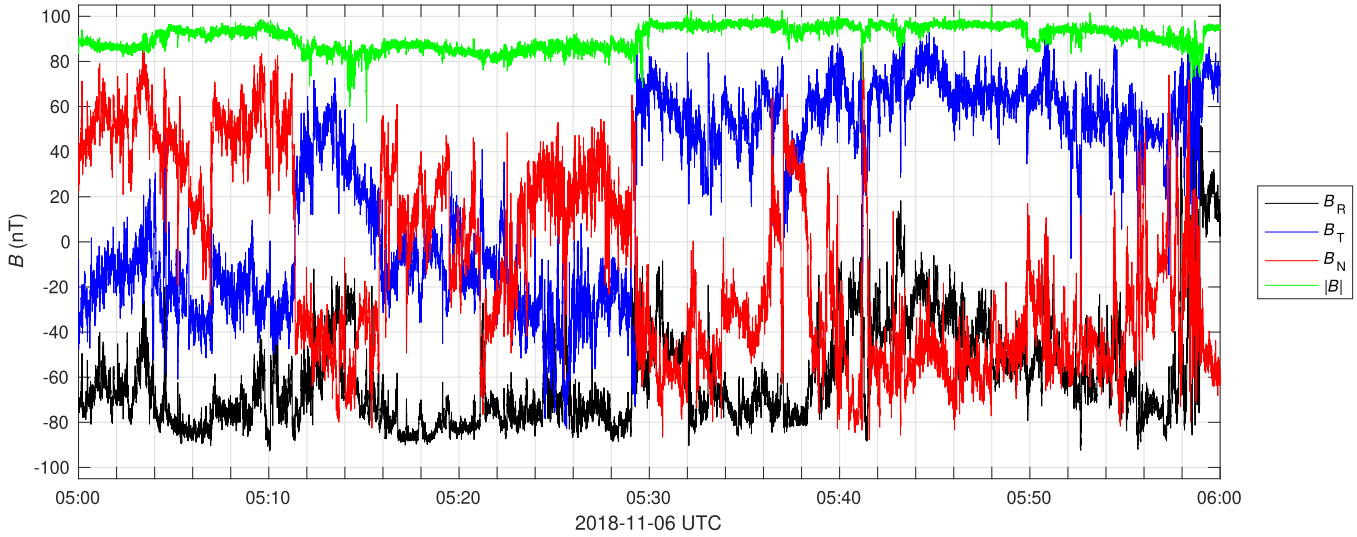

Figure 5. Magnetic field components and magnitude as measured by PSP/FIELDS during one hour near first perihelion (2018 November 6, 0500–0600 UT) at radius 36 $R_\odot$, at the full sampling frequency of 299 Hz. Short-term fluctuations are mostly Alfvénic in the sense of conserving $|B|$. Domains of nearly constant $|B|$ are often separated by minute-scale changes in $|B|$ and sharp, major jumps in the components of B. We argue that these separate domains of magnetic pressure-balanced Alfvénic fluctuations could correspond to flocculation mixing layers.

which can be used to estimate a likely range of turbulent fluctuations. This range of turbulence values, when superposed on the resolved simulation variables, provides an estimate of the full range of likely magnetic and velocity components along the PSP trajectory during the first encounter. The resulting range of predicted values agrees reasonably well with the range of fluctuations suggested by the averaged PSP data. For example, focusing on the radial component of $\boldsymbol{B}$ in Figure 4, the range of expected values accounts for the possibility of numerous switchbacks.

Based on these considerations and prior evidence, one may anticipate that the fluctuations become large in and near the Alfvén critical zone. Sufficiently large fluctuations, particularly in the Alfvén mode (Matteini et al. 2018) can produce large deflections including reversals of magnetic polarity, i.e., switchbacks. Previous studies focused mainly on the presence of large-amplitude fluctuations, while here we point out a number of other characteristics of PSP data that require further study.

It is also useful to take a closer look at the PSP data near perihelion to motivate the more detailed analysis that follows. Figure 5 provides an example of magnetic field data for one hour near the first perihelion. Here we see that the magnetic field components show large fluctuations. The radial component is predominantly negative, but shows sporadically large clusters of fluctuations (Chhiber et al. 2020). Meanwhile, the magnetic field displays a structure consisting of regions of relatively constant magnetic field strength separated by sharp changes. At high temporal cadence, we can identify a few regions in which the main (radial) magnetic field changes polarity for brief times; these are the switchbacks.

4.2. Radial Velocity Shear, Alfvén Speed, and Conditions Near Shear Instability

A key element of the shear-driving hypothesis is the conversion of initially more ordered but inhomogeneous flows into more randomized flows, a conversion that must occur in the presence of ordered magnetic fields. This is a scenario that can explain the transition from striation to flocculation in the STEREO images (DeForest et al. 2016). As discussed in Section 2.3, a uniform magnetic field will resist Kelvin–Helmholtz-like roll-ups when the velocity differential is less than the local Alfvén speed. Therefore we need to examine quantitative features of the plasma flows in comparison with the local Alfvén speed. To establish the context, we begin by computing the Alfvén speed from the PSP data, which we show for the first two encounters (E1 and E2) in Figure 6. Four levels of averaging are shown, over 1, 4, 12, and 24 hr. The salient feature is that there is considerable variation of Alfvén speed in both encounters, with values around 80 to 110 km s^{-1} near first perihelion, with higher values close to 200 km s^{-1} near second perihelion, and with values as low as $\sim$10 km s^{-1} at greater distance from the Sun.

As a next step we examine the radial velocity, normalized to the Alfvén speed, for E1. This is motivated by Chandrasekhar's condition for suppression, $V_A > \Delta V$, where ΔV is an appropriate measure of the velocity contrast across a shear layer. (In the current complex environment, we view that a physically relevant value of the Alfvén speed V_A would be an appropriate regional average.) However, we emphasize that here we are not looking for conditions for subsequent linear instability, since the additional signatures we examine would indicate a *past* instability closer to the Sun rather than an imminent instability. Nevertheless, we do not rule out that subsequent instability may take place, particularly because, as mentioned above, polarity reversals are observed further from the Sun and there is evidence that their frequency may actually increase with increasing radial distance (Macneil et al. 2020; Owens et al. 2020). The presence of velocity changes over relatively short distances that exceed the local Alfvén speed is an indication that the criterion for Kelvin–Helmholtz rollup is likely to be reached in this region (or it may even be in progress as we observe it), something that cannot be ascertained with single-point measurements.

In Figure 7 (top), we show the radial plasma velocity of solar wind protons. Two resolutions are shown, one in which V_A is computed at 0.87 s resolution, and the other using 1 hr smoothed (running averaged) V_A. There are numerous

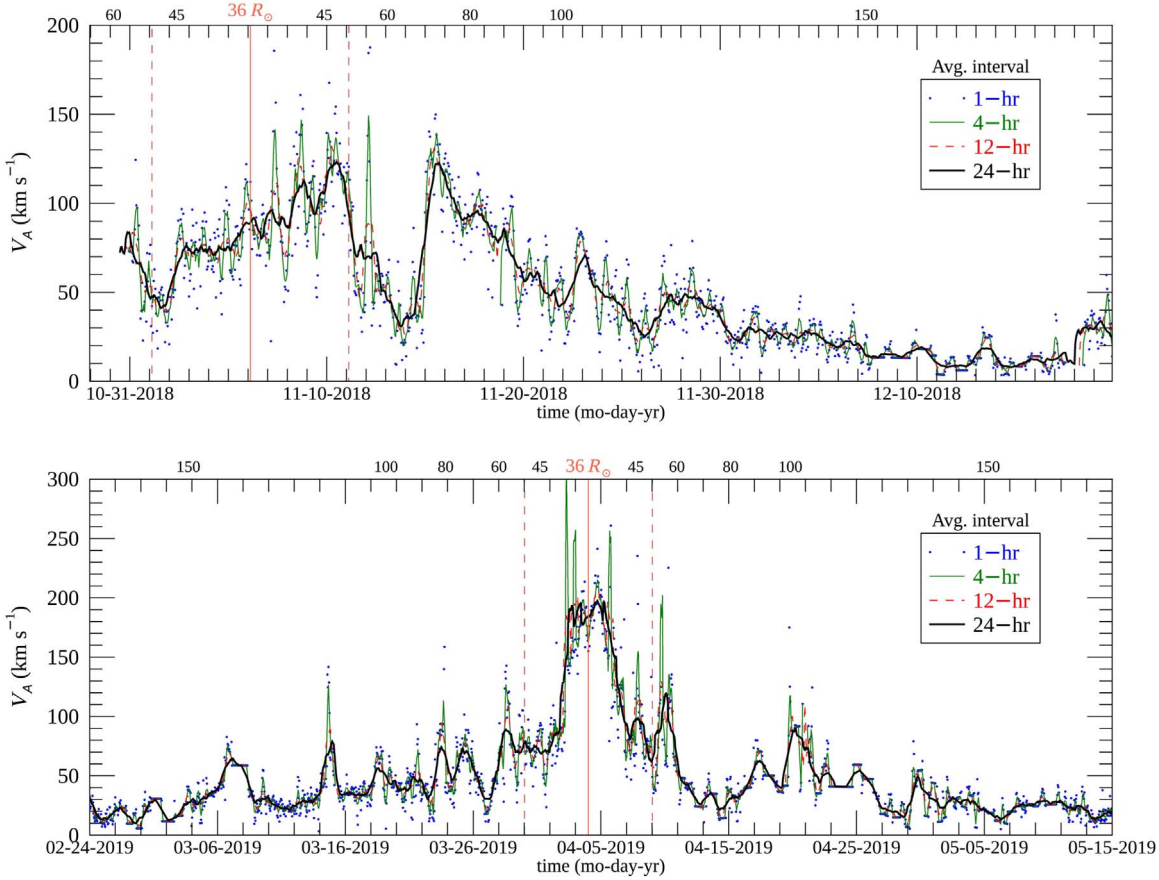

Figure 6. Alfvén speed vs. time computed at four levels of coarse graining during parts of the (top) first and (bottom) second PSP orbit. The data are plotted at 1 hr cadence in each case, while averaging is performed over a moving window of specified duration. The red vertical lines mark the respective perihelia, and the dashed vertical lines demarcate a period of 10 days centered on the perihelia. Selected heliocentric distances of PSP are marked above the upper horizontal axes.

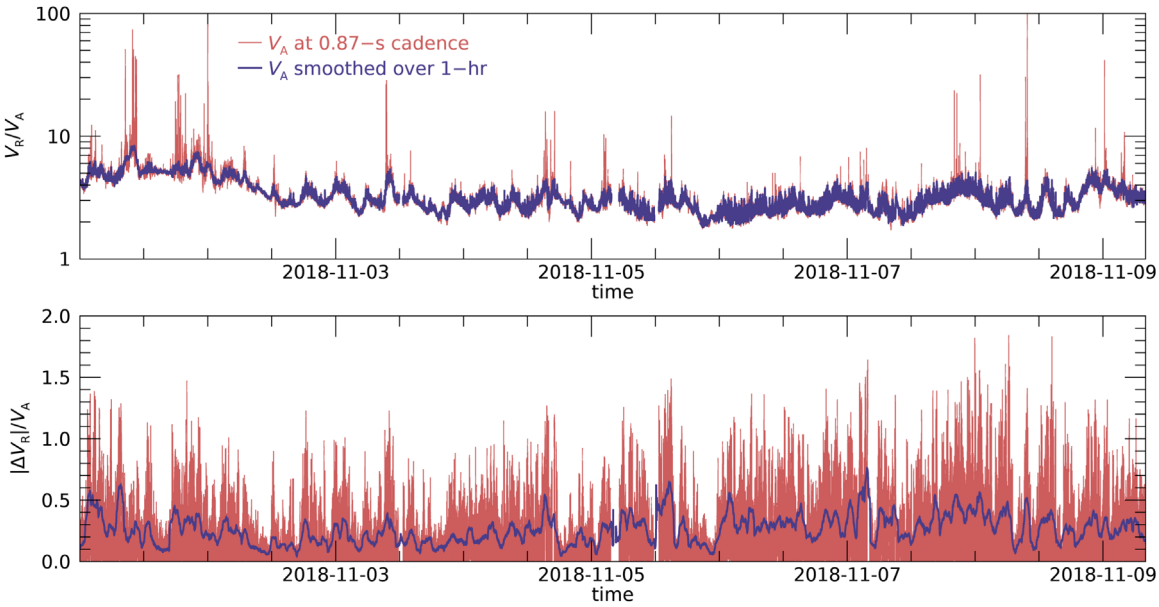

Figure 7. (Top) Radial velocity of solar wind protons in Alfvén speed units, near the first PSP perihelion. Radial speed is sampled at a cadence of 1 NYs $\approx$ 0.87 s, and normalized either by the 1 NYs Alfvén speed or the 1 hr running average of the Alfvén speed, as indicated. (Bottom) Red curve shows the absolute value of increments $\Delta V_R = V_R(t+\tau) - V_R(t)$ of the radial velocity V_R computed from 0.87 s data and for a time lag of $\tau = 10$ min, approximately the correlation time in this part of the PSP orbit (see Parashar et al. 2020). Also shown is the 1 hr rms of ΔV_R (blue curve). The increments are normalized by the 1 hr moving average of V_A. It is apparent that there are many intermittently distributed V_R-increments that exceed the local (smoothed) Alfvén speed.

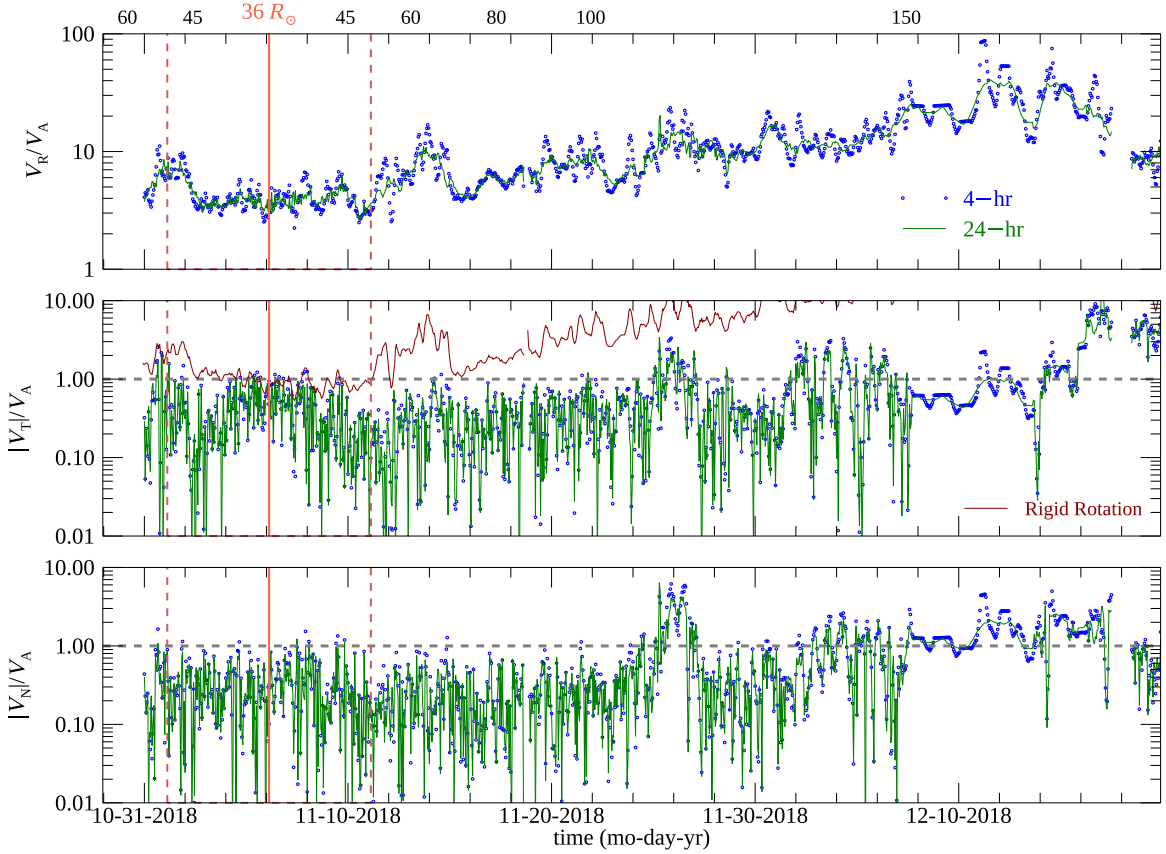

Figure 8. Proton velocity components in (coarse-grained) Alfvén speed units during the first PSP orbit. Two levels of coarse-grained Alfvén speed are used (4- and 24 hr moving averages), while the proton velocities are plotted at 1 hr cadence. The brown curve in the middle panel shows the speed of rigid rotation in units of the 4 hr moving average of V_A. This would be the tangential speed of the plasma if it were corotating with the Sun, with angular speed corresponding to the sidereal rotation period of 24.47 days. Selected heliocentric distances of PSP are marked above the upper horizontal axis.

variations of V_R that are larger than one or a few Alfvén speeds, but we must ask at what scales these occur. To that end, we compute the increments of the observed radial component of plasma velocity, normalized in an analogous way to the 1 hr moving average of V_A. The increment is defined as $\Delta V_R = V_R(t+\tau) - V_R(t)$ with time lag τ. The value $\tau = 10$ minutes is selected, corresponding to the typical measured correlation time in the first encounter (Parashar et al. 2020), which is expected to be a typical large-scale magnetic flux tube size. Therefore, the measured increments are estimates of velocity contrasts ΔU between adjacent flux tubes as suggested in Figure 3. We see that ΔV_R frequently exceeds V_A. This is a way to assess the likelihood of nearby nonlinear K-H activity. We conclude that the case for the development of a mixing layer is reasonably well supported.

4.3. Transverse Velocity and Fluctuation Components

The behavior of the transverse velocity components is also significant and may exhibit signatures of plasma rollup, a process that also involves convection of the magnetic field. In the idealized case, the magnetic field resists the rollup, and is amplified as it is distorted by the velocity shear (Miura 1982; Goldstein et al. 1989; Roberts et al. 1992; Malagoli et al. 1996). If there were little or no transverse velocity initially, one would expect that the maximum excursion of the transverse velocity would be, roughly speaking, bounded by the local (amplified) Alfvén speed, according to the typical condition of equipartition of energy between magnetic and flow energies in the solar wind frame.

To examine the excursion of the transverse velocities, Figures 8 and 9 show the three Cartesian components of velocity normalized to the locally averaged Alfvén speed during the first and second orbits, respectively. It is apparent that the two transverse components V_T and V_N are almost always nicely bounded by the local Alfvén speed. To be specific, among 1 s values of $|V_T|/V_A$ and $|V_N|/V_A$ from the first encounter, about 7% exceeded 1 and none exceeded 4. Note that a 2 hr moving average of V_A was used to obtain these percentages.

Figures 8(b) and 9(b) also indicate the speed of rigid rotation with the Sun at the sidereal rotation period of 24.47 d (Pécseli 2020), which is plotted in units of the 4 hr moving average of V_A (brown curves). It can be seen that, at times near both the first and second perihelia, V_T was comparable to the speed of corotation with the Sun.

The probability distributions of the longitudinal velocity component V_T for E1 are shown at three positions along the orbit in Figure 10. We note that the distribution for the inbound orbit, 6 days prior to perihelion, shows a multi-component distribution with several distinct peaks (Figure 10(a)). Each peak covers a spread in V_T that resembles a separate sub-distribution. From the time series (not shown), these are seen to result from time periods in which V_T fluctuates about positive or negative values for durations from a fraction of an hour to a few hours; longer durations are more common at greater

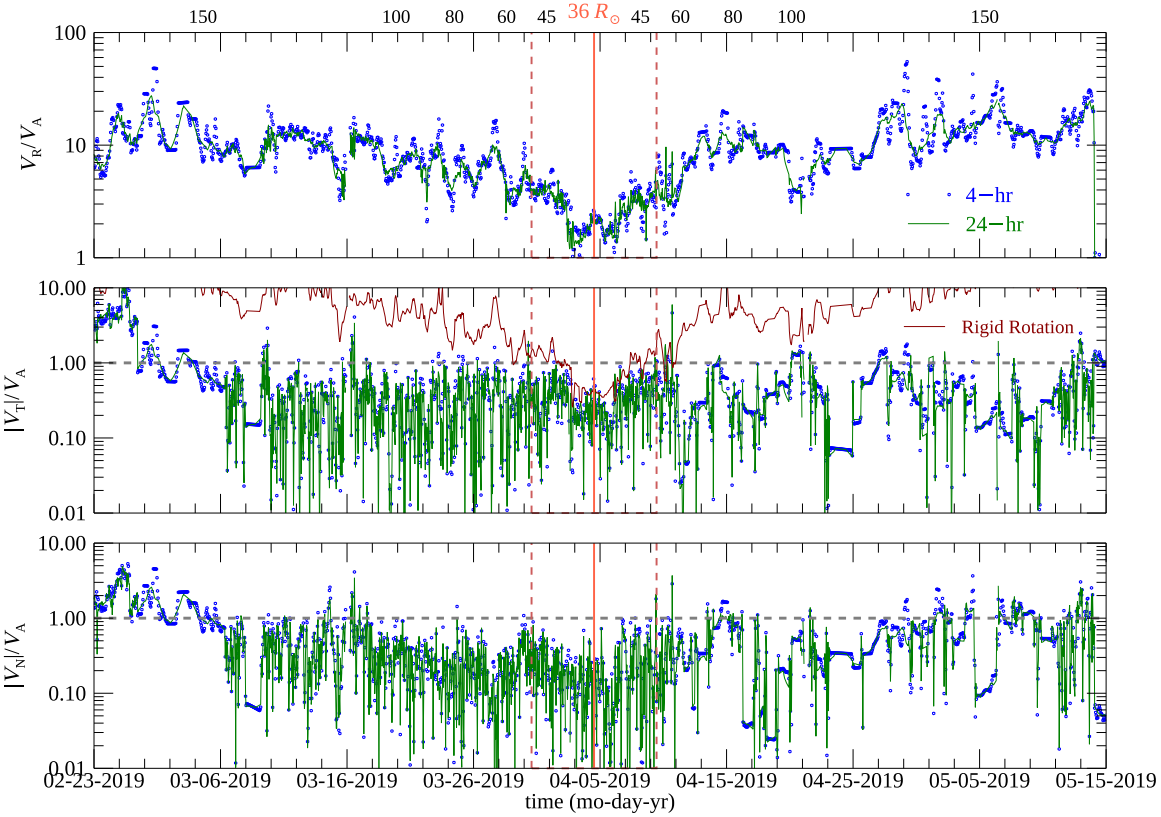

Figure 9. Proton velocity components in (coarse-grained) Alfvén speed units during the second PSP orbit. See caption of Figure 8 for more details.

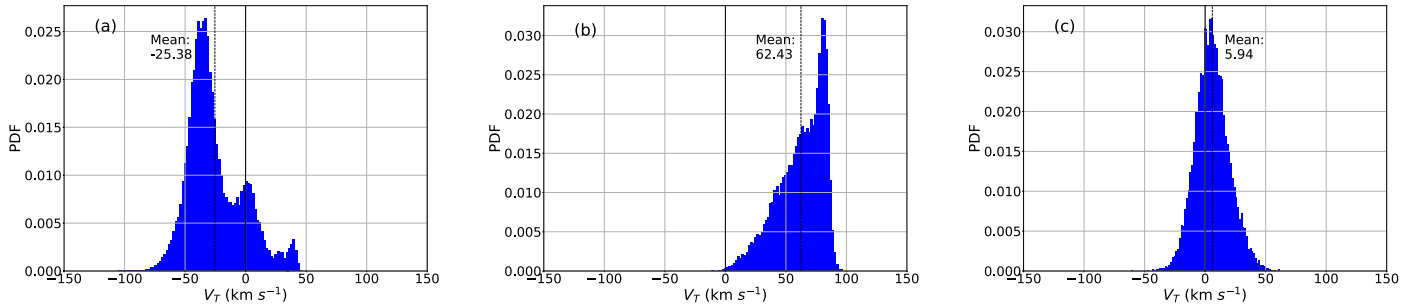

Figure 10. (a) Probability distribution function (PDF) of longitudinal solar wind velocity V_T (in km s^{-1}) as measured by PSP with a cadence of 1 NYs (≈0.87 s) during 2018 October 31, 0800–1600 UT, about 6 days before first perihelion. The vertical dashed line indicates the mean value. During this and other time periods far from perihelion, V_T is randomly distributed around zero, with sub-distributions around positive or negative values for up to a few hours (as seen here mostly at negative values). (b) Similar PDF for 2018 November 6, 0000–0800 UT, including the time of first perihelion. Near perihelion, V_T is clearly biased toward positive values, indicating partial corotation with the Sun. (c) Similar PDF for 2018 November 11, 0000–0800 UT, or 5 days after first perihelion. Far from perihelion, V_T is again randomly distributed around zero.

distance from the Sun. The 8 hr time period shown in Figure 10(a) happens to have more negative values. Near perihelion, the distribution shows a strong bias toward positive V_T (Figure 10(b)) at speeds comparable to the corotation velocity of around 70 km s^{-1}. There is again a broad distribution, in this case skewed toward smaller values. Five days after perihelion, for the example period shown in Figure 10(c), the distribution is centered roughly about $V_T = 0$ with a single strong maximum. The distributions of the latitudinal component V_N for E1 (not shown) are qualitatively similar except they do not exhibit a bias toward positive values near perihelion.

In the corona, the nascent solar wind is expected to be channeled along magnetic flux tubes that corotate with the Sun in the longitudinal direction. Thus the PSP observations near first perihelion are consistent with partial corotation in that the longitudinal solar wind velocity V_T fluctuates around the corotation speed while the latitudinal component V_N fluctuates around zero. These observed patterns are also evident in Figure 4, where the global simulation variables (u_θ, u_φ) correspond to PSP velocity components ($-V_N$, V_T). We refer to partial corotation because, according to Figure 10(b), most of the solar wind has V_T below the corotational value of ≈70 km s^{-1}. Indeed, such "slippage" of solar wind elements from corotation is expected to occur beyond the Alfvén critical zone where the magnetic field no longer controls the solar wind flow. Therefore, we interpret the observation of partial corotation near the first perihelion as evidence that PSP was already close to the Alfvén critical zone. Farther from the Sun, there is no apparent corotation of the solar wind (see Figures 4 and 10) and

such slippage becomes complete. However, near first perihelion the partial corotation indicates partial slippage, and suggests that neighboring magnetic flux tubes could have substantially different V_T values. In other words, in addition to the radial velocity shear suggested in Figure 3 and Section 4.2, there could also be longitudinal velocity shear associated with partial corotation.

Intriguingly, in Figure 10(b), part of the V_T distribution is actually faster than the corotational speed, which could be attributed to Kelvin–Helmholtz roll-ups in the mixing layer outside the Alfvén critical zone. These interpretations of large reported V_T need to be viewed as tentative, given that modeling has so far not been able to reproduce V_T values as large as those discussed here.

4.4. Domains and Anisotropy of Alfvénic Fluctuations

Ever since the seminal work of Belcher & Davis (1971), it has been recognized that magnetic and velocity fields in the solar wind tend to fluctuate together, which has been attributed to an Alfvén mode

$$\boldsymbol{v} = \pm \frac{\boldsymbol{b}}{\sqrt{\mu_0 \rho}}, \tag{3}$$

where $\boldsymbol{v} \equiv \boldsymbol{V} - \boldsymbol{V}_0$ and $\boldsymbol{b} \equiv \boldsymbol{B} - \boldsymbol{B}_0$, subtracting any large-scale (mean) fields $\boldsymbol{V}_0$ and $\boldsymbol{B}_0$, ρ is the mass density, and the right-hand side is the magnetic fluctuation expressed in terms of the Alfvén speed. Even at large amplitudes, such fluctuations are solutions of the incompressible MHD equations (Moffatt 1978). If there is a mean magnetic field $\boldsymbol{B}_0$, then the $+$ sign indicates propagation along $-\boldsymbol{B}_0$ and the $-$ sign indicates propagation along $\boldsymbol{B}_0$.

For compressible MHD, large-amplitude propagating solutions exist for the Alfvén mode so long as the total field magnitude $|B| = |(\boldsymbol{B}_0 + \boldsymbol{b})|$ is uniform (Barnes & Hollweg 1974; Goldstein et al. 1974; Barnes 1979). However, note that the divergence requirement on the magnetic field limits the spatial region over which this "incompressible" mode can exist (Barnes 1979). From the work of Belcher & Davis (1971) and many others, in situ measurements of solar wind fluctuations throughout the heliosphere have indicated that such Alfvénic fluctuations are predominantly outward. In PSP data, such fluctuations are common and frequently of large amplitude, with $|b| \sim |B|$ (see, e.g., Figure 2 of Kasper et al. 2019). Parashar et al. (2020) and Horbury et al. (2020) recently described several measures of Alfvénicity as applied to the PSP E1 data. Other aspects of Alfvénic fluctuations have also gained recent attention (Matteini et al. 2018; Matteini et al. 2019; D'Amicis et al. 2020).

The nearly constant magnetic field magnitude $|B|$ (a distinctive property of Alfvénic fluctuations) is often evident in PSP data as illustrated in Figure 5. For such cases, in terms of its components, the vector $\boldsymbol{B}$ is randomly walking on a sphere of nearly constant $|B|$, as described by Barnes (1981). In turbulence, constant magnetic pressure may be associated with rapid, local relaxation processes that also favor patches of flow-field alignment, as in Equation (3) (Matthaeus et al. 2008; Osman et al. 2011). Matteini et al. (2015) offer an alternative view of constancy of $|B|$, namely, that it is associated with conservation of ion kinetic energy in the reference frame of observed alpha particle motion.

As can be seen from Figure 5, PSP data from the first encounter reveal Alfvénic domains with nearly constant $|B|$ that are often separated by sharp, major jumps in the components of $\boldsymbol{B}$, as necessary to preserve the divergence condition $\nabla \cdot \boldsymbol{B} = 0$ when $\nabla \cdot \boldsymbol{V} \neq 0$. Another indication of the domain structure comes from probability distribution functions (PDFs) of $|B|$ as shown in Figure 11. It is clear that 8 hr samples near perihelion are likely to contain one to a few regions of nearly constant magnetic field. This is consistent with Alfvénic turbulence, but in addition, it is consistent with mixing-layer dynamics, as we shall see below.

At the interface between two plasma flows with relative shear, once the condition $\Delta V > V_A$ is met, Kelvin–Helmholtz dynamics are possible. This develops into a mixing layer that eventually includes roll-ups and magnetic polarity reversals (switchbacks; Malagoli et al. 1996), and the mixing layer is expected to grow with distance along the flow, or in this case with distance from the Sun. Now, in our hypothesis (see Figure 3), there are numerous magnetic flux tubes in the nascent solar wind. Some of the interfaces between these should develop the Kelvin–Helmholtz instability and mixing layers. These mixing layers should grow until they come into contact. When they do, it is possible that they merge in the sense that the shear-driven dynamics (i.e., flocculation) homogenizes the magnetic pressure within the merged region. We interpret the domains of Alfvénic turbulence with nearly constant $|B|$ as such (possibly merged) mixing layers, and they exhibit sharp boundaries as topological defects across which the dynamics have not yet balanced the magnetic pressure. PSP data also provide some evidence that these domains become larger with increasing heliocentric distance r, as expected for mixing layers that grow and merge. In Figure 11(c), we see a case 5 days after first perihelion when a very narrow distribution of nearly constant $|B|$ was observed for an entire 8 hr period, in contrast with the 8 hr period near first perihelion in which multiple distributions were observed (Figure 11(b)). As described earlier for V_T, sub-distributions in the time series for $|B|$ that last several hours are more common at increased r several days away from perihelion, while the variation in PSP travel speed was relatively minor.

In Figure 5, we see that at some times within a domain of nearly constant $|B|$, in association with particularly strong magnetic fluctuations, $|B|$ temporarily decreases for up to a few minutes before returning back to the same nearly constant level. At such times the magnetic pressure balance is temporarily disrupted within the domain. Sudden drops in $|B|$ have previously been reported during switchbacks, i.e., reversals in B_R (Bale et al. 2019; Kasper et al. 2019). Here we note that a temporary decrease in $|B|$ can occur together with strong fluctuations in *any* of the magnetic field components, e.g., in Figure 5 at hour 5.37 or 5.63, and are not particular to switchbacks. This is consistent with the view that many switchbacks belong to a continuum of fluctuations that can occur in all field components as part of in situ dynamics in the solar wind.

To examine the Alfvénic magnetic fluctuations in more detail, we calculated statistics of magnetic increments $\boldsymbol{\Delta B} = \boldsymbol{B}(t + \tau) - \boldsymbol{B}(t)$ for time lags τ of 1 s, 10 s, 1 min, 10 min, 1 hr, and 6 hr. (Note that the FIELDS instrument typically samples the magnetic field at 299 Hz, so even the 1 s lag is much longer than the instrumental resolution.) In order to study the fluctuation anisotropy, we decomposed the magnetic

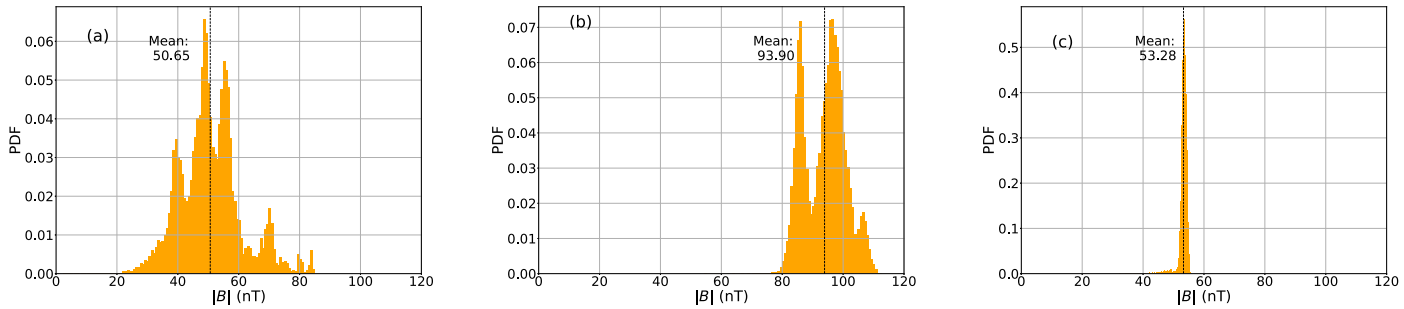

Figure 11. (a) PDF of magnetic field magnitude $|B|$ (in nT) as measured by PSP sampled at a cadence of 1 NYs (≈0.87 s) during 2018 October 31, 0800–1600 UT, about 6 days before first perihelion. Vertical dashed line indicates mean value. Clumps in the distribution of $|B|$ correspond to local flux tubes. (b) Similar PDF for 2018 November 6, 0000–0800 UT, including the time of first perihelion. The mean of $|B|$ was generally larger when PSP was closer to the Sun. (c) Similar PDF for 2018 November 11, 0000–0800 UT, or 5 days after first perihelion. At this location, the entire 8 hr period effectively comprises a single domain.

increments into a parallel component $\Delta B_\parallel$ along the magnetic field $\boldsymbol{B}(t)$ and two components along basis vectors perpendicular to $\boldsymbol{B}(t)$, in the R-T plane (ΔB_1, a roughly longitudinal increment) and perpendicular to the R-T plane (ΔB_2, a roughly latitudinal increment). We calculated the variances (mean squares) of these quantities as a measure of the scale-dependent fluctuation energy in these components. To measure the conservation of $|B|$, we also calculated the variance of increments in $|B|$.

The variance ratio of the magnitude increment to the total increment, $\langle(\Delta|B|)^2\rangle/\langle(\boldsymbol{\Delta B})^2\rangle$, usually remained below 0.05 throughout both the first and second PSP orbits, only rarely exceeding 0.2, for all values of τ. This confirms the basically Alfvénic nature of the fluctuations. Throughout both orbits, there were some special time periods with an unusually low ratio, i.e., especially good magnetic pressure balance. It turns out that such special time periods occurred near both the first and second perihelia, i.e., during 2018 November 3–10 and during 2019 April 3–6. We display results for this ratio and ratios between variances of increment components, as a function of time lag τ, for these special times near the first and second perihelia and also for the entire data sets of the first orbit (2018 October 6 to 2018 December 19) and second orbit (2019 February 20 to 2019 May 15) in Figure 12.

This figure shows that the variance ratio of the magnitude increment to the total increment (blue curves) is indeed lower for the special periods near first perihelion (a) and second perihelion (c) compared with the full orbits (b and d). Yet even for data from the full orbits, the ratio for lags up to 1 h remains below 0.025, confirming the near constancy of $|B|$ and magnetic pressure over such timescales. At $\tau = 6$ h, the ratio increases, indicating that this timescale is frequently greater than the domain duration; even so, the ratio remains below 0.06.

The ratio of the parallel increment variance to total increment variance (red curves) is also quite low (<0.1) for the 1 s time lags, and it grows larger for longer time lags according to the near constancy of $|B|$ and the increase in the increment amplitude $|\Delta B|$ for increasing lag τ. For a small amplitude ($|\Delta B| \ll |B|$), we would expect $\Delta B_\parallel \approx \Delta|B|$. However, for large-amplitude Alfvén mode fluctuations that maintain constant $|B|$, i.e., for spherical polarization in which $\boldsymbol{B}$ remains on a sphere in its component space, $\Delta B_\parallel$ is directly related to the fluctuation amplitude. Here this geometric effect dominates over the actual magnitude fluctuations, with $\langle(\Delta B_\parallel)^2\rangle \gg \langle(\Delta|B|)^2\rangle$ even for our smallest (1 s) lags.

A surprising result from this analysis is an anisotropy between the two perpendicular components of the magnetic field increment. The variance ratio of roughly longitudinal to latitudinal perpendicular increments, $\langle(\Delta B_1)^2\rangle/\langle(\Delta B_2)^2\rangle$, ranges from 1.4 to 2 for the longest (6 hr) lags while decreasing to about 1 for the shortest (1 s) lags. The transition seems to relate to the correlation time of several minutes. This anisotropy for long lags persists throughout both orbits, though on average it is particularly strong during time periods with better magnetic pressure balance such as the times close to perihelia. As such it does not appear to be related to the direction of the PSP orbital motion, which varies strongly and systematically throughout the orbit.

This anisotropy of magnetic increments for long τ is unlikely to originate in or below the inner corona, in which the latitudinal and longitudinal directions are not strongly distinguished. It can be understood in terms of velocity shear above the Alfvén critical zone between flux tubes with varying degrees of longitudinal corotation, leading to perpendicular field increments that are predominantly longitudinal over large scales and then isotropize after a turbulent cascade to smaller scales.

4.5. Cross-Helicity and Signatures of Velocity Shear

In terms of a volume average, here designated as $\langle\cdots\rangle$, the cross-helicity may be defined as

$$H_c \equiv \langle \boldsymbol{v}\cdot\boldsymbol{b}\rangle = \frac{1}{4}(Z_+^2 - Z_-^2), \tag{4}$$

where the fluctuations in magnetic field are computed in Alfvén units as $\boldsymbol{b} = (\boldsymbol{B} - \boldsymbol{B}_0)/\sqrt{\mu_0\rho}$, and the Elsässer energies are $Z_+^2 = \langle|\boldsymbol{v} + \boldsymbol{b}|^2\rangle$ and $Z_-^2 = \langle|\boldsymbol{v} - \boldsymbol{b}|^2\rangle$. The traditional view is that the ± Elsässer fluctuations $\boldsymbol{z}^\pm = \boldsymbol{v} \pm \boldsymbol{b}$ comprise wave packets that propagate either along the $\boldsymbol{B}_0$ direction ($\boldsymbol{z}^-$), or opposed to it ($\boldsymbol{z}^+$). This definition corresponds to and generalizes the large-amplitude eigenmodes described in the previous section (see Equation (3)). H_c is an ideal invariant of the incompressible MHD system and has significance whether or not a mean magnetic field $\boldsymbol{B}_0$ is present.

It is well known that, in the inner heliosphere, solar wind fluctuations have a strong cross-helicity in the sense that propagation is dominantly outward (Belcher & Davis 1971). In our simple cartoon (Figure 3), if all the magnetic field is outward and the fast outward streams are located in the flux tubes with weaker magnetic field, then the cross-helicity of long-wavelength fluctuations will be negative and they will travel outward except in switchback regions. If the prevailing

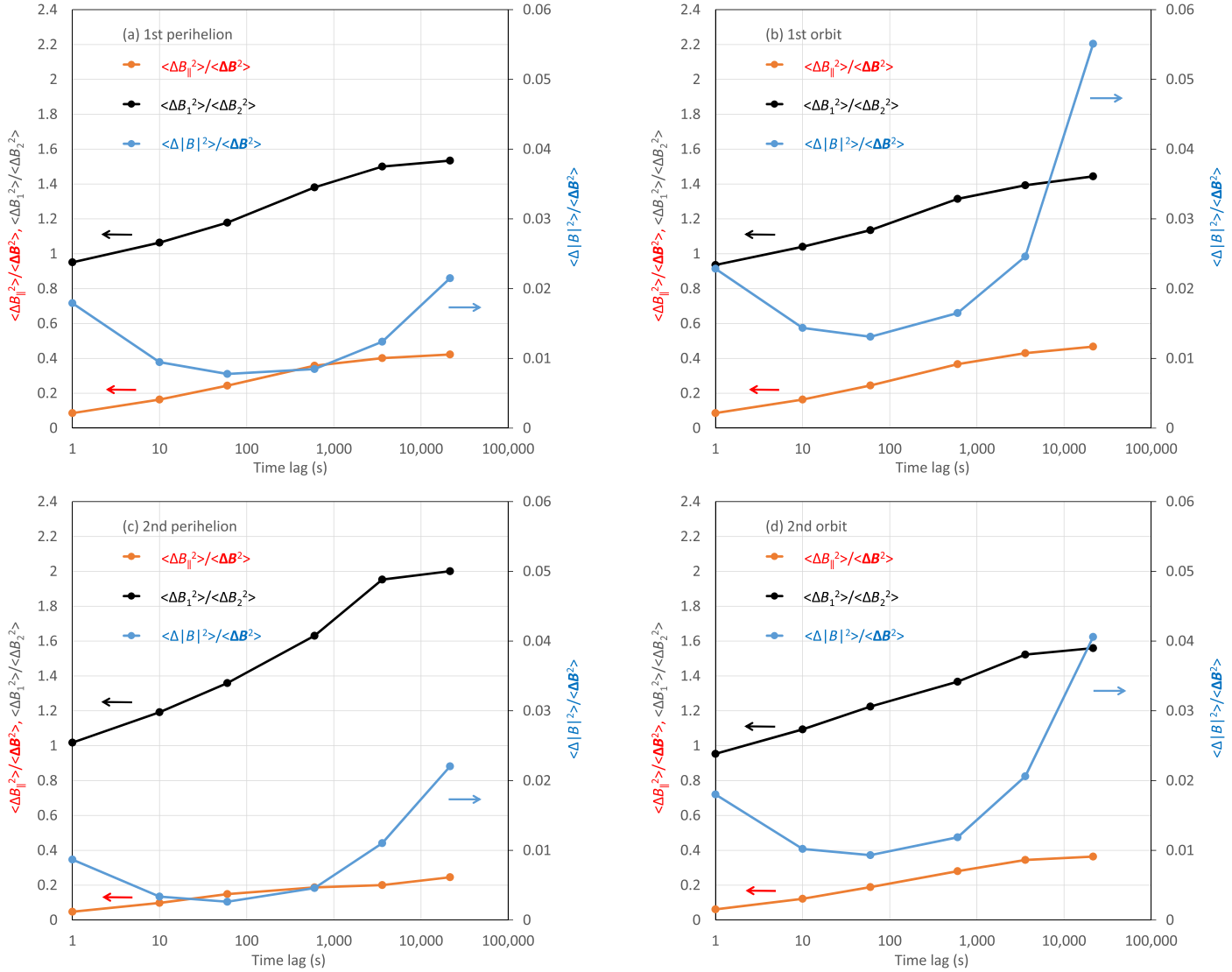

Figure 12. Ratios of variances of magnetic field increments measured by PSP (a) near first perihelion, 2018 November 3–10, (b) during first orbit, from 2018 October 6 to 2018 December 19, (c) near second perihelion, 2019 April 3–6, and (d) during second orbit, from 2019 February 20 to 2019 May 15. For varying time lags τ, vector magnetic increments $\boldsymbol{\Delta B} = \boldsymbol{B}(t+\tau) - \boldsymbol{B}(t)$ are calculated and decomposed into a component $\Delta B_\parallel$ parallel to $\boldsymbol{B}(t)$ (mostly radial) and two perpendicular components, ΔB_1 in the R-T plane (mostly longitudinal) and ΔB_2 out of the R-T plane (mostly latitudinal). The magnitude increment ($\Delta|B|$) is also calculated. The low variance ratios of the magnitude increment and parallel increment to the total increment (blue and red curves, respectively) indicate the near constancy of $|B|$ and magnetic pressure, a characteristic of Alfvénic fluctuations. The variance ratio of longitudinal to latitudinal increments (black curves) is between 1.4 and 2 for the longest (6 hr) increments but decreases to about 1 for the shortest (1 s) increments. The anisotropy of longer time increments is unlikely to originate in or below the inner corona, and can be attributed to longitudinal velocity shear near the Alfvén critical zone due to partial corotation, leading to perpendicular field increments that are predominantly longitudinal over large scales and isotropize after a turbulent cascade to smaller scales.

magnetic polarity is inward (as it is during E1 and E2), in the context of our cartoon, the faster streams should still be in the weaker flux tubes, to give a positive cross-helicity and the observed outward propagation. In a more complete description of the solar wind, there is also likely to be a broadband spectrum of more standard outward-propagating Alfvénic fluctuations.

In PSP observations close to the Sun, the cross-helicity measured by the ratio $\sigma_c = (Z_+^2 - Z_-^2)/(Z_+^2 + Z_-^2)$ is generally quite large, suggestive of a preponderance of outward traveling Alfvén waves. There are departures from Alfvénicity for increments at small lags, including reduced cross-helicity, as reported by Parashar et al. (2020). At the same time, our present analysis shows that the magnetic magnitude increment is quite small for small time lags (Figure 12), which is consistent with mostly Alfvén mode fluctuations. This could be because, above the conventional Alfvén point, velocity shears can begin supplying turbulence energy (Zank et al. 1996; Breech et al. 2008) that remains nearly incompressible but not entirely outward-directed.

5. Results: 3D Compressible MHD Simulation of Mixing-layer Dynamics

Having examined several plasma and magnetic field diagnostics in the PSP data, we now turn to the results of more local compressible MHD simulations, emphasizing points of comparison with the observations. We seek to examine further possible points of consistency with plasma dynamics driven by nonlinear mixing-layer dynamics as envisioned in Section 2.3 for the transition between striation and flocculation outside the Alfvén critical zone.

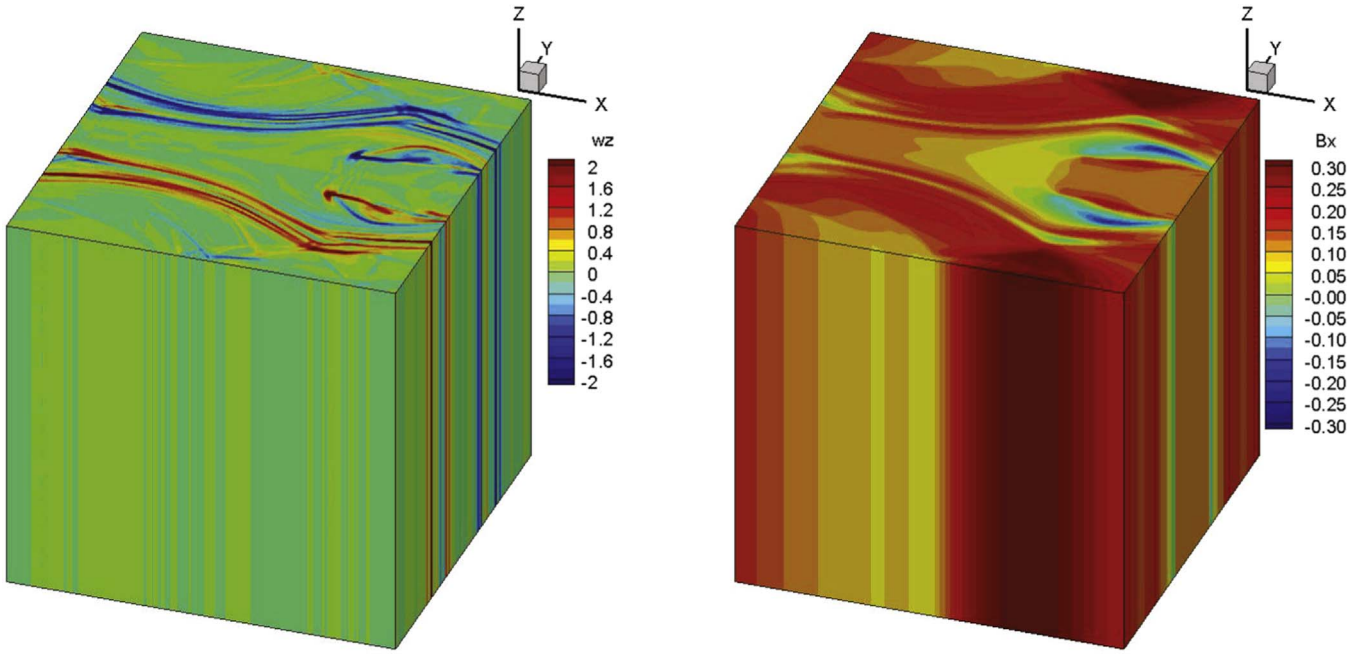

Figure 13. (Left) Vorticity in the z-direction and (right) magnetic field in the x-direction (shown by color scales) from 3D compressible MHD simulation at $t = 120$. Vortex rollup, inhibited by the magnetic field, is just beginning to take effect. Initially flow reversal occurred across two thin planes at $y = L_y/4$ and $3L_y/4$ and the magnetic field was initially entirely in the $+x$-direction, stronger outside those two planes and weaker between them.

5.1. Compressible MHD Simulation Results

We carried out a number of compressible MHD runs using the approach outlined in Section 3.3. The unperturbed initial state in all cases is based on two periodic planar shear layers between regions of colinear magnetic field that change strength across the same regions as the shear layers. Therefore the sheetlike regions of electric current density approximately coincide with layers of vorticity. This is to emulate in a simple way the juxtapositioning of parallel flux tubes with varying axial velocity fields, as suggested in Figure 3. We choose this simple shear configuration to test our hypothesis in a simple form: Can organized flows and magnetic fields that are initially oriented in one direction give rise to Kelvin–Helmholtz dynamics and plasma signatures such as those observed by PSP? In the actual solar wind, as we have pointed out, there is at least partial corotation in the longitudinal direction (see Section 4.3) and, we believe, also some slippage of individual flux tubes and longitudinal velocity shear as well (see Section 4.4).

The baseline parameters corresponding to the results shown here were given in Table 1. Different runs (not shown) were done in two dimensions and in three dimensions, with varying velocity contrast ΔU across the shear layers, and several values of uniform B_x in the strong and weak magnetic field regions. Within the range of parameters that were varied, the results were all similar; therefore we show just one case in the diagnostics here, as described in Table 1.

Beginning from the initial state described above, the dynamics proceed along the lines of a hydrodynamic mixing layer. The initially planar vorticity layers distort due to the early stages of vortex rollup. The magnetic field is too weak to prevent the distortion from reaching macroscopic dimensions. A snapshot of this state is shown in the two panels of Figure 13, where the breakup of the vortex layers begins along with large magnetic field directional deflections and small regions of weak field in which the polarity reverses. Figure 14 describes the state of the system later, at simulation time $t = 290$, when the shear-driven dynamics are more fully developed and clearly in a nonlinear stage. In particular, the phenomenon of roll-ups has noticeably emerged, where the vortex layers have folded. Shocklets have formed at locations at which the flow direction change is relatively abrupt. Perhaps most importantly, there are now large transverse velocities in both the positive and negative $\hat{y}$ (vertical) directions. The large deflected motions have carried along the magnetic field (right panel), which also exhibits large transverse deflections. Examination of the sign and magnitude of the streamwise $\hat{x}$-direction magnetic field (indicated by the color legend) indicates the presence of regions of polarity reversals, or "switchbacks." Here these are entirely caused by nonlinear instability driven by the initial shear layers.

A complementary graph of the magnetic field components is shown in Figure 15 for time $t = 290$ of the MHD simulation. The spatial structure is sampled as a function of distance s along a trajectory at an 18° angle relative to the axes of the box that threads through the (periodic) box several times, to produce a one-dimensional series that spans about 10 correlation lengths, similar to the PSP data sample shown in Figure 5. For reasons to be discussed shortly, we associate the x-direction along the mean field in the simulation with the $-R$ direction for PSP measurements, and the y-direction with the T direction, so the left panel uses $B_R = -B_x$ and $B_T = B_y$. Note the region of approximately constant $|B|$ and the presence of switchbacks in the simulation plot, in qualitative accord with the PSP data.

We will now show several diagnostics that permit a quantitative comparison of several features of the simulation and the observations by PSP. We do not expect precise correspondence because the simulation setup is a vast oversimplification of the interplanetary physical system. But if our conjectures are correct concerning the basic physics that

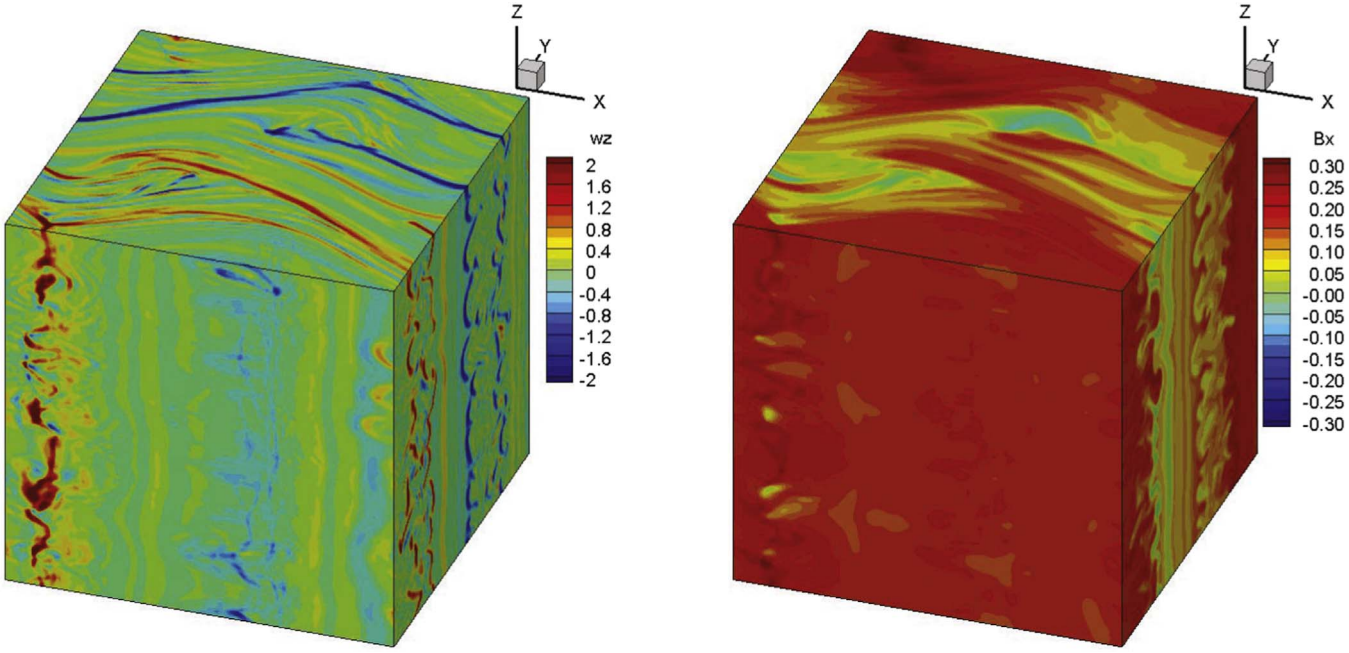

Figure 14. (Left) Vorticity in the z-direction and (right) magnetic field in the x-direction (shown by color scales) from 3D compressible MHD simulation at a later time, $t = 290$. Vortex rollup is now well developed, producing two switchback regions, which recur intermittently throughout the simulation run.

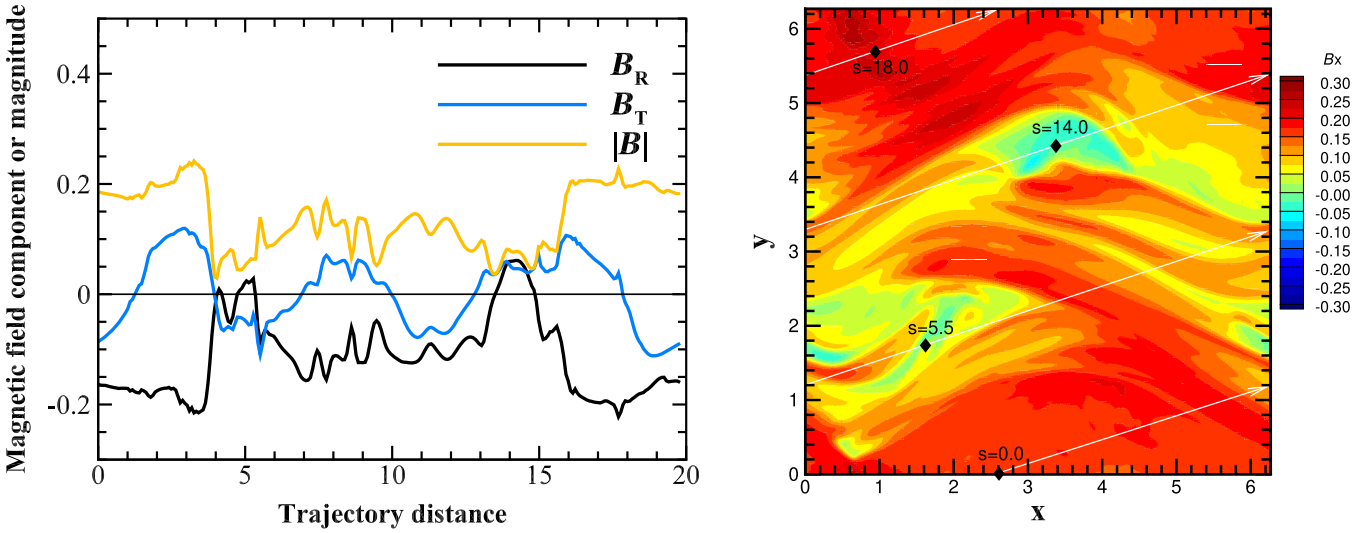

Figure 15. (left) Magnetic field components and magnitude from the 3D compressible MHD simulation at time $t = 290$. Note the presence of "switchbacks," i.e., reversals of B_R, as well as large symmetric fluctuations of transverse B_T. The magnetic field magnitude $|\boldsymbol{B}|$ is relatively constant within regions delineated by the proximity of switchbacks. This figure can be qualitatively compared with Figure 5. (right) The simulation plane and trajectory employed to obtain the data in the left panel. The trajectory is drawn, annotated with reference distances s.

drives the evolution in the solar wind, then we might find some consistency in the comparisons.

5.2. Comparison with PSP Data: Magnetic Field Magnitude

A special property of large-amplitude Alfvén waves, a constant magnitude $|B|$, is apparently a familiar property in MHD turbulence. Constant-magnitude patches or regions have also been observed in PSP data, as shown for the first PSP encounter in Figures 5 and 11. An analysis of the shear-driven MHD simulation results also shows a similar distribution of magnetic field magnitude, as illustrated in Figure 16. Note that, at the earlier time, $t = 120$, the distribution has peaks associated with the initial conditions, in which $|B|$ was concentrated at two initial values, shown by vertical dotted-dashed lines at 0.08 and 0.18. These peaks have smoothed somewhat by the later time $t = 290$, representing a more developed dynamical state that we consider comparable to the solar wind at initial PSP perihelia, somewhat downstream of the Alfvén critical zone. Even at the later simulation time, one observes in the PDF of $|B|$ the presence of preferred values of $|B|$ or sub-distributions as seen in the PSP data.

5.3. Comparison with PSP Data: Magnetic Switchbacks

Considerable attention has been given to the appearance of switchbacks in the PSP data (Bale et al. 2019; Dudok de Wit et al. 2020) where, as mentioned earlier, they are seen more

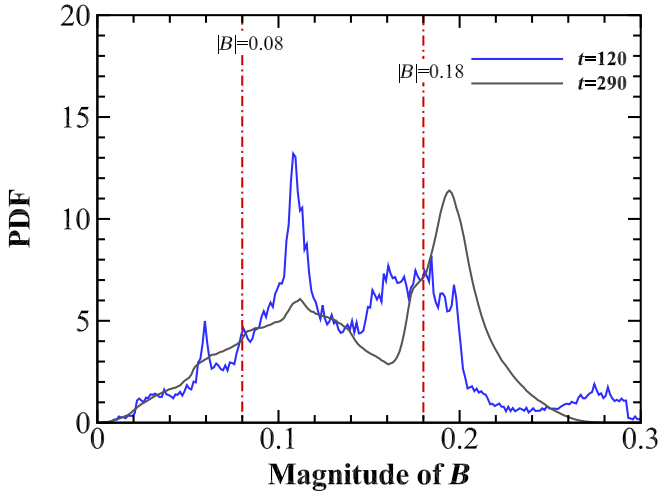

Figure 16. PDF of magnetic field magnitude from the 3D compressible MHD simulation at simulation times $t = 120$ and $t = 290$. Initial magnetic field values are annotated. This figure can be qualitatively compared with Figure 11(b).

dramatically near perihelion than in the more distant solar wind. While many switchbacks are seen in the first orbit, as in Figure 2, a close up look at one hour of data, as in Figure 5, shows that most of the solar wind is filled with unipolar negative radial field.

For the present purposes, it is of interest to compare the frequency of occurrence of reversed-polarity magnetic fields in the presence of a dominant magnetic polarity and strong shear. In this way, one can compare switchbacks from PSP with magnetic polarity reversals in our standard MHD simulation, noting that, for most of E1 and E2, the large-scale magnetic field at PSP was nearly in the $-R$ direction, which we associate with the x-direction along the mean field in the simulation, whereas a PSP measurement of a transverse component such as T corresponds to the component along y, the direction that cuts across shear layers in the simulation. To this end, we compute the distribution of the radial magnetic field component B_R from 8 hr of PSP data near first perihelion (2018 November 6, 0000–0800 UT) and compare this to the distribution of $B_R \equiv -B_x$ from the simulation at two times. This comparison is presented in the two panels of Figure 17.

The qualitative features of these distributions are quite similar: The PSP data show one strong peak at a dominant negative polarity, with a shelf-like distribution that extends to positive polarity values, indicating switchbacks. In the simulation, there are two preferred values of dominant polarity at the earlier time shown, and a single strong peak at the later time that we believe better represents the more developed dynamics downstream of the Alfvén critical zone. At both times, the simulation shows a relatively flat, low-level, shelf-like distribution of reversed polarity, much like the observed distribution in the left panel.

The simulation data in Figure 17, as well as analysis of several other simulations we have carried out, demonstrate that switchbacks occur with similar frequencies in MHD mixing-layer dynamics and in the PSP data near first perihelion.

5.4. Comparison with PSP Data: Transverse Velocities

The PSP results shown above demonstrate that the transverse velocity components near first PSP perihelion are essentially bounded by the local or neighborhood value of the Alfvén speed. It is also interesting, using the same normalization, to compare the distribution of the V_T component of velocity in the PSP data with the corresponding "nonradial" (transverse) component V_y of the plasma velocity in the MHD simulation data. One can see in Figure 18 that the local Alfvén speed represents an approximate limit that constrains the dynamics in both the simulation and PSP observations, which is consistent with the reasoning above (see Section 4.3).

6. Discussion and Conclusions

Motivated by STEREO observations (DeForest et al. 2016), we have examined the possibility that shear-driven dynamics drive the transition from elongated, or striated, structures in the lower corona to more isotropic, or flocculated, structures above the Alfvén critical zone. The associated release of energy in the sheared flows represents an additional source of energy over and above the preexisting Alfvénic turbulence originating at lower coronal altitudes. If the above hypothesis is correct, this transition signals an enhancement in outer scale turbulence energy that persists to much larger heliocentric distances. This hypothesis has been examined here beginning with clues from imaging, and further motivated by the large turbulence amplitudes seen in global MHD simulations. PSP provides an opportunity to begin detailed analysis of the consequences of the shear-driving hypothesis. The first results of this analysis have been presented in some detail here.

The basic picture is that of a magnetized parallel mixing layer in which the velocity contrasts are large enough to cause significant deflections and even reversals of the magnetic field. The salient features of the mixing layer are well known in hydrodynamic, engineering, and practical applications; a common example is shown in Figure 19. The magnetic field parallel to the flow presents a complication in that it resists deflection. However, as anticipated in theory (Chandrasekhar 1981; Miura & Pritchett 1982) and demonstrated in simulations (Goldstein et al. 1989; Roberts et al. 1992; Malagoli et al. 1996; Landi et al. 2006), a sufficiently strong shear in comparison with the ambient Alfvén speed will produce the typical Kelvin–Helmholtz-type roll-ups. We show that, in principle, episodic switchbacks can be accounted for by in situ solar wind dynamics, not requiring nonradial inputs from the Sun or its inner corona.

The heliospheric simulations that confirm the likelihood of such conditions in the solar wind are consistent with a number of previous observations (Borovsky 2016; Horbury et al. 2018; Usmanov et al. 2018; Lockwood et al. 2019). Indeed the expected amplitude of turbulent fluctuations inferred from turbulence modeling suggests that large-amplitude departures from the laminar state, including switchbacks, may be anticipated as PSP perihelia migrate inward toward the Alfvén critical zone. It is also important to recognize that the fluctuations that propagate and convect outward from the lower corona and into the critical zone from below may not be uniform or homogeneous. In fact, it is well established in observations that the vertical velocity of fluctuations may vary considerably, with typical variations due to type II spicules (De Pontieu et al. 2009) in the range of 50–100 km s^{-1}. Similar contrasts in radial velocity are seen throughout the inner corona in analysis of deep exposure STEREO-A/COR2 coronagraph images (DeForest et al. 2018). These types of fluctuations may also cause magnetic

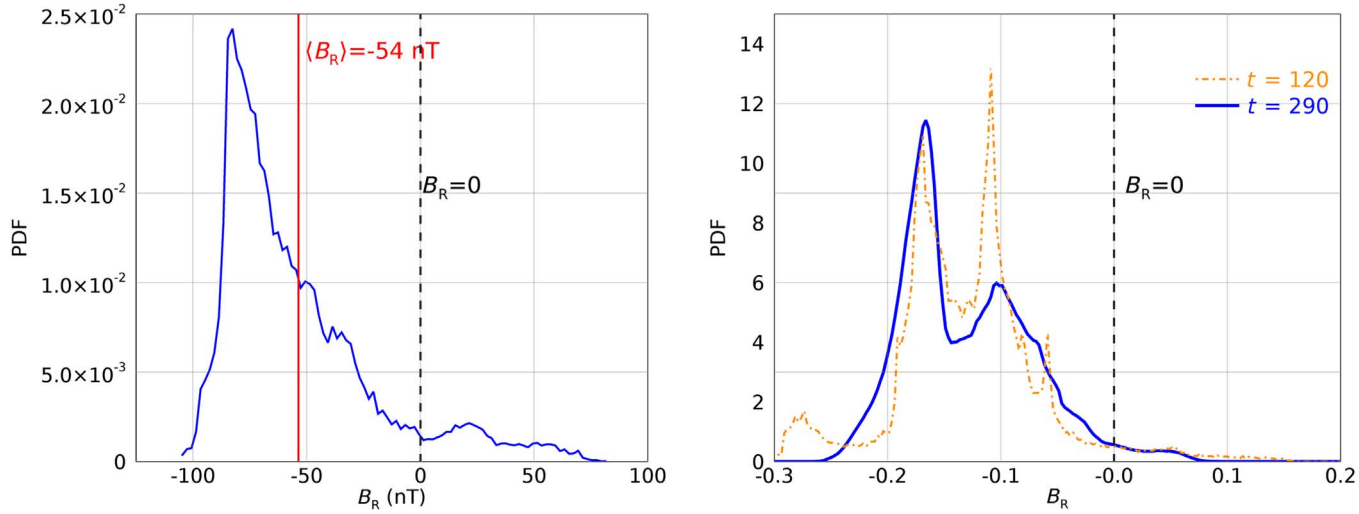

Figure 17. (Left) PDF of radial magnetic field from 8 hr of data that include PSP's 1st perihelion; (right) PDF of "radial" x-component of magnetic field at two times from the shear-driven 3D compressible MHD simulation.

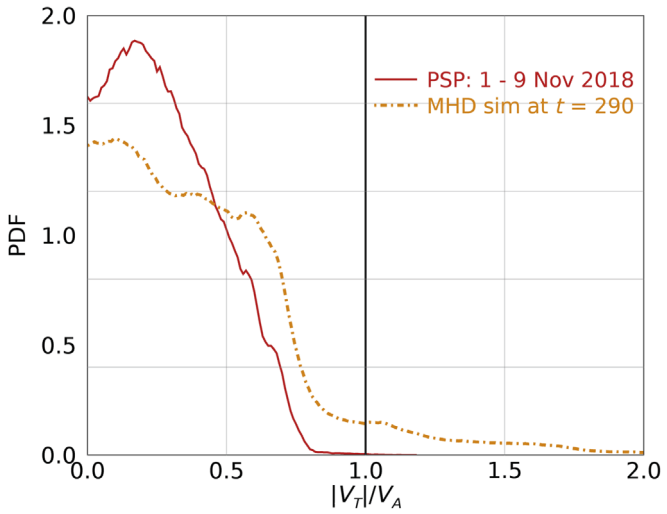

Figure 18. Solid red curve shows the PDF of the transverse velocity normalized to the 1 hr running average of the Alfvén speed during the first PSP encounter. Dash-dotted orange curve shows the PDF of the transverse velocity from the shear-driven 3D compressible MHD simulation, normalized to the local Alfvén speed. Compare with Figures 8 and 9.

Figure 19. Images of plumes above smokestacks in Newark, Delaware, USA with escaping vapors exhibiting a sequence of changes analogous to what is envisioned for the shear-driven dynamics of the young solar wind. Upon escape from the constraining smokestack, the plume is initially well-collimated. Roll-ups are initiated near the edges due to shear. At greater distances, the plumes become wider and more isotropic.

reversals (Samanta et al. 2019) that might propagate upward and possibly survive to the Alfvén critical zone (Tenerani et al. 2020). If they do survive to the Alfvén critical zone, these fluctuations would be expected, under the right detailed conditions, to contribute to driving of turbulence through nonlinear instability.

PSP now has made several passes through the outer parts of this region, and provides substantial data relevant to the present suggestions. Here we have examined the time series, and the distributions of magnetic field magnitude, radial magnetic field, and transverse velocities. All of these appear to be consistent with expectations and simulation results for a shear-driven dynamics scenario. Furthermore, the domains of Alfvénic fluctuations are consistent with mixing layers that grow and/or merge with distance from the Alfvén critical zone, and we find anisotropy among the perpendicular magnetic increments with stronger longitudinal increments at large scales, which seems unlikely to arise from deep in the solar corona but could be explained in terms of longitudinal velocity shear associated with partial corotation.

As an additional step to test this hypothesis, we carried out 3D high Mach number compressible MHD simulations as driven by an initial planar velocity shear layer with a parallel sheared magnetic field and a velocity contrast of three times the Alfvén speed. Vortex rollup and nonlinear Kelvin–Helmholtz activity is anticipated and observed. As expected, the magnetic field is deflected, sometimes through large angles. Reversals of the field direction, corresponding to the phenomenon of "switchbacks" in the PSP observations, are seen with similar frequency in the simulations and in the observations. The distributions of transverse velocity, radial magnetic field, and magnetic field magnitude all show

similarities between the simulation results and PSP observations from the first encounter.

Several features of the PSP observations are related to the familiar appearance of high cross-helicity states (Alfvénicity) in the inner heliosphere (Belcher & Davis 1971; Bruno & Carbone 2013), as well as their familiar sense of polarization associated with a predominantly outward-propagating character. Large-amplitude Alfvén waves of pure polarization are required to be "spherically polarized" with the magnetic amplitude wandering on a constant-magnitude surface (Barnes & Hollweg 1974). Ordinarily one would associate such states with incompressibility. Indeed, even though the magnetosonic Mach numbers exceed unity here, the density fluctuations are observed to be small (Krupar et al. 2020), presumably because the Alfvéncity is large enough to prohibit proliferation of compressive modes. Furthermore, we observed that the magnitude of the magnetic field is relatively constant in patches. This may be an additional indicator of large-scale flux tube structures originating in the lower corona and subsequent mixing layers, where transverse pressure balance is approximately realized due to quasi-two-dimensional turbulent relaxation (Servidio et al. 2008).

Another interesting feature of the observations relates to the outward-propagating polarization of the cross-helicity, viewed in the context of the idealized configuration illustrated in Figure 3. Below the Alfvén critical zone, substantial cross-helicity can be present in the vertical (axial) magnetic field of the flux tubes and the excess radial (axial) velocity found in some magnetic flux tubes. Both of these features are inferred from coronagraph observations (DeForest et al. 2018). It is interesting that, to maintain a sense of outward propagation at the scale of the (model) flux tubes in a unipolar region, the faster flowing flux tubes must coexist with weaker axial magnetic fields, while flux tubes with slower radial speeds would have stronger radial magnetic fields. This sense of correlation remains the same whether the unipolar region has positive or negative radial magnetic field. This sense may dominate for other reasons; for example, strong closed fields may inhibit acceleration of the nascent solar wind. Apparently the regions with opposite sense of polarization, i.e., those that correspond to inward propagation, are not present at significant levels during the PSP first perihelion, which lies outside the Alfvén critical zone. This situation may change when PSP passes through or below the critical zone. For example, the inward-type modes may build up in the critical zone due to sharp Alfvén speed gradients or due to stagnation.

It appears that velocity differences between flux tubes may be available, under the right conditions, to drive large-amplitude fluctuations that are responsible for the transition between striation in the sub-Alfvénic inner corona and flocculation in the super-Alfvénic outer corona. This phenomenon may be characteristic of what we may reasonably call the "young solar wind." The region in which this appears to occur is outside the Alfvén critical zone and near the first $\beta = 1$ zone. This is where pressure fluctuations become large enough to overcome the rigidity of the magnetic field. Vortex roll-ups and large deflections or switchbacks of the magnetic field become possible. From the first detailed examination of the relevant evidence presented here, it appears that this hypothesis is reasonable, or at least not ruled out.

The injection of additional turbulence energy due to shear-induced rollup may set the scale of the energy-containing eddies in the region of injection, thus determining the turbulence correlation length observed from about 40 $R_\odot$ outward to 1 au and beyond. In this regard, the potential for a significant additional injection of energy outside the Alfvén critical zone may act as an "afterburner" that further boosts heating and acceleration.

While the evidence summarized above appears to support the mixing-layer hypothesis, it does not diminish the potential importance of large-amplitude fluctuations that originate in the lower corona, propagate outward, and survive into the region where mixing-layer dynamics occur. Such fluctuations could be generated by field line stirring and reconnection in the photospheric "furnace" that produces braiding of field lines, nanoflares, and a turbulent cascade that is probably responsible for heating the corona and accelerating the wind to supersonic and super-Alfvénic speeds (McKenzie et al. 1995; Axford et al. 1999; Matthaeus et al. 1999; Cranmer et al. 2007; Verdini et al. 2010). There could also be ejecta from large-scale interchange reconnection (Fisk & Kasper 2020) or wavelike fluctuations launched from spicules (Samanta et al. 2019). Some fluctuations of these types originating from lower altitudes may also produce local large-angle magnetic deflections. We suspect that it will be difficult to rule out contributions to large angular deflections due to several potential sources. In any case, such fluctuations, upon arrival in the Alfvén critical zone, would contribute to the perturbations that unleash the nonlinear magnetized mixing-layer phenomena that we describe here.

Predictions for future perihelia. As perihelia move closer and then enter the Alfvén critical zone, we expect to observe a further increase in both the mean magnetic field and the amplitude of broadband turbulence. As we move closer to the region of "striations," the more random fluctuations seen due to roll-ups should give way to more organized patterns of near-radially aligned flux tubes. These striations contain the velocity shears and magnetic shears that provide the energy for the roll-ups further along. Approaching these more organized magnetic structures, we expect the frequency of switchbacks to decrease, and the sharpness of velocity jumps to increase as the sub-Alfvénic region is approached, assuring greater confinement, and the suppression of Kelvin–Helmholtz-like mixing-layer dynamics. The amplitude and frequency of occurrence of large fluctuating tangential velocity should decrease, while periods of corotation should become more frequent as the plasma at lower altitudes comes under increasing control of the more rigid lower coronal magnetic field. In this same region, PSP may begin to see other signatures, for example, component reconnection between adjacent striated flux tubes, or indications of helical field lines within them. It is possible that, if PSP perihelia lie deep enough in the corona, the striated flux tubes may display properties such as Beltrami, Alfvénic, and force-free signatures that are indicative of approach to a generalized relaxed state of turbulence (Servidio et al. 2008). This is directly analogous to our compressible MHD simulation results at very early times and the behavior of familiar smoke plumes near the confining smoke pipes as seen in Figure 19.

In this paper, we have presented a hypothesis regarding the role of shear-driven dynamics in the region currently explored by PSP as well as supporting evidence. As a logical consequence, we develop a set of expectations for what

PSP will observe as its perihelia explore deeper in the Alfvén critical zone and below. These predictions will soon be tested. In any case, approaching these regions for first-ever in situ observation, PSP is expected to reveal important features of the plasma, electromagnetic, and energetic particle environment in the solar corona that shape the entire heliosphere.

The authors are grateful to Wiwithawin Charoenngam for plotting assistance. This work utilizes data produced collaboratively between AFRL/ADAPT and NSO/NISP. This research has been supported in part by grant RTA6280002 from Thailand Science Research and Innovation and the Parker Solar Probe mission under the ISOIS project (contract NNN06AA01C) and a subcontract to University of Delaware from Princeton University (SUB0000165). M.L.G. acknowledges support from the Parker Solar Probe FIELDS MAG team. Y.Y. and M.W. acknowledge support from NSFC (Grants 11672123, 11902138, and 91752201). Additional support is acknowledged from the NASA LWS program (NNX17AB79G) and the HSR program (80NSSC18K1210 & 80NSSC18K1648).

ORCID iDs

D. Ruffolo https://orcid.org/0000-0003-3414-9666
W. H. Matthaeus https://orcid.org/0000-0001-7224-6024
R. Chhiber https://orcid.org/0000-0002-7174-6948
A. V. Usmanov https://orcid.org/0000-0002-0209-152X
Y. Yang (杨艳) https://orcid.org/0000-0003-2965-7906
R. Bandyopadhyay https://orcid.org/0000-0002-6962-0959
T. N. Parashar https://orcid.org/0000-0003-0602-8381
M. L. Goldstein https://orcid.org/0000-0002-5317-988X
C. E. DeForest https://orcid.org/0000-0002-7164-2786
A. Chasapis https://orcid.org/0000-0001-8478-5797
B. A. Maruca https://orcid.org/0000-0002-2229-5618
M. Velli https://orcid.org/0000-0002-2381-3106
J. C. Kasper https://orcid.org/0000-0002-7077-930X

References

Arge, C. N., Henney, C. J., Koller, J., et al. 2010, in AIP Conf. Ser. 1216, Twelfth International Solar Wind Conference, ed. M. Maksimovic et al. (Melville, NY: AIP), 343
Axford, W. I., & McKenzie, J. F. 1992, in Proc. Solar Wind Seven Coll., ed. E. Marsch & R. Schwenn (Oxford: Pergamon), 1
Axford, W. I., McKenzie, J. F., Sukhorukova, G. V., et al. 1999, SSRv, 87, 25
Bale, S. D., Badman, S. T., Bonnell, J. W., et al. 2019, Natur, 576, 237
Bale, S. D., Goetz, K., Harvey, P. R., et al. 2016, SSRv, 204, 49
Balogh, A., Forsyth, R. J., Lucek, E. A., Horbury, T. S., & Smith, E. J. 1999, GeoRL, 26, 631
Barnes, A. 1979, in Solar System Plasma Physics, ed. E. N. Parker, C. F. Kennel, & L. J. Lanzerotti (Amsterdam: North-Holland), 249
Barnes, A. 1981, JGR, 86, 7498
Barnes, A., & Hollweg, J. V. 1974, JGR, 79, 2302
Bavassano, B., Dobrowolny, M., Mariani, F., & Ness, N. F. 1982, JGR, 87, 3617
Belcher, J. W., & Davis, L., Jr. 1971, JGR, 76, 3534
Borovsky, J. E. 2016, JGRA, 121, 5055
Breech, B., Matthaeus, W. H., Minnie, J., et al. 2008, JGRA, 113, A08105
Bruno, R., & Carbone, V. 2013, LRSP, 10, 2
Chandrasekhar, S. 1981, Hydrodynamic and Hydromagnetic Stability (New York: Dover)
Chhiber, R., Goldstein, M. L., Maruca, B. A., et al. 2020, ApJS, 246, 31
Chhiber, R., Usmanov, A. V., DeForest, C. E., et al. 2018, ApJL, 856, L39
Chhiber, R., Usmanov, A. V., Matthaeus, W. H., & Goldstein, M. L. 2019a, ApJS, 241, 11
Chhiber, R., Usmanov, A. V., Matthaeus, W. H., Parashar, T. N., & Goldstein, M. L. 2019b, ApJS, 242, 12
Cranmer, S. R., van Ballegooijen, A. A., & Edgar, R. J. 2007, ApJS, 171, 520
Crooker, N. U., Kahler, S. W., Larson, D. E., & Lin, R. P. 2004, JGRA, 109, A03108
Dahlburg, R. B., Boncinelli, P., & Einaudi, G. 1998, PhPl, 5, 79
D'Amicis, R., Matteini, L., Bruno, R., & Velli, M. 2020, SoPh, 295, 46
Davies, L., & Gather, U. 1993, J. Am. Stat. Assoc., 88, 782
De Pontieu, B., McIntosh, S. W., Hansteen, V. H., & Schrijver, C. J. 2009, ApJL, 701, L1
DeForest, C. E., Howard, R. A., Velli, M., Viall, N., & Vourlidas, A. 2018, ApJ, 862, 18
DeForest, C. E., Matthaeus, W. H., Viall, N. M., & Cranmer, S. R. 2016, ApJ, 828, 66
Dudok de Wit, T., Krasnoselskikh, V. V., Bale, S. D., et al. 2020, ApJS, 246, 39
Einaudi, G., Boncinelli, P., Dahlburg, R. B., & Karpen, J. T. 1999, JGR, 104, 521
Fisk, L. A., & Kasper, J. C. 2020, ApJL, 894, L4
Fox, N., Velli, M., Bale, S., et al. 2016, SSRv, 204, 7
Goldstein, M. L., Klimas, A. J., & Barish, F. D. 1974, in Solar Wind Three, ed. C. T. Russell (Greenbelt, MD: NASA), 385
Goldstein, M. L., Roberts, D. A., Ghosh, S., & Matthaeus, W. H. 1987, ESA Spec. Publ., 275, 115
Goldstein, M. L., Roberts, D. A., & Matthaeus, W. H. 1989, GMS, 54, 113
Hickmann, K. S., Godinez, H. C., Henney, C. J., & Arge, C. N. 2015, SoPh, 290, 1105
Hollweg, J. V. 1974, JGR, 79, 1539
Horbury, T. S., Matteini, L., & Stansby, D. 2018, MNRAS, 478, 1980
Horbury, T. S., Woolley, T., Laker, R., et al. 2020, ApJS, 246, 45
Kahler, S. W., Crooker, N. U., & Gosling, J. T. 1996, JGR, 101, 24373
Kasper, J. C., Abiad, R., Austin, G., et al. 2016, SSRv, 204, 131
Kasper, J. C., Bale, S. D., Belcher, J. W., et al. 2019, Natur, 576, 228
Krupar, V., Szabo, A., Maksimovic, M., et al. 2020, ApJS, 246, 57
Landi, S., Hellinger, P., & Velli, M. 2006, GeoRL, 33, L14101
Landi, S., Velli, M., & Einaudi, G. 2005, ApJ, 624, 392
Lau, Y. Y., & Liu, C. S. 1980, PhFl, 23, 939
Lockwood, M., Owens, M. J., & Macneil, A. 2019, SoPh, 294, 85
Lotova, N. A., Blums, D. F., & Vladimirskii, K. V. 1985, A&A, 150, 266
Lotova, N. A., Vladimirskii, K. V., & Obridko, V. N. 2011, SoPh, 269, 129
Macneil, A. R., Owens, M. J., Wicks, R. T., et al. 2020, MNRAS, 494, 3642
Malagoli, A., Bodo, G., & Rosner, R. 1996, ApJ, 456, 708
Matteini, L., Horbury, T. S., Pantellini, F., Velli, M., & Schwartz, S. J. 2015, ApJ, 802, 11
Matteini, L., Stansby, D., Horbury, T. S., & Chen, C. H. K. 2018, ApJL, 869, L32
Matteini, L., Stansby, D., Horbury, T. S., & Chen, C. H. K. 2019, NCimC, 42, 16
Matthaeus, W. H., Pouquet, A., Mininni, P. D., Dmitruk, P., & Breech, B. 2008, PhRvL, 100, 085003
Matthaeus, W. H., Zank, G. P., Oughton, S., Mullan, D. J., & Dmitruk, P. 1999, ApJL, 523, L93
McComb, W. D. 1990, The Physics of Fluid Turbulence (New York: Oxford Univ. Press)
McKenzie, J. F., Banaszkiewicz, M., & Axford, W. I. 1995, A&A, 303, L45
Michel, F. C. 1967, JGR, 72, 1
Miura, A. 1982, PhRvL, 49, 779
Miura, A., & Pritchett, P. L. 1982, JGR, 87, 7431
Moffatt, H. K. 1978, Magnetic Field Generation in Electrically Conducting Fluids (New York: Cambridge Univ. Press)
Mozer, F. S., Agapitov, O. V., Bale, S. D., et al. 2020, ApJS, 246, 68
Müller, D., Marsden, R. G., St., Cyr, O. C., Gilbert, H. R. & The Solar Orbiter Team 2013, SoPh, 285, 25
Osman, K. T., Wan, M., Matthaeus, W. H., Breech, B., & Oughton, S. 2011, ApJ, 741, 75
Owens, M., Lockwood, M., Macneil, A., & Stansby, D. 2020, SoPh, 295, 37
Parashar, T. N., Goldstein, M. L., Maruca, B. A., et al. 2020, ApJS, 246, 58
Pécseli, H. L. 2020, Series in Plasma Physics: Waves and Oscillations in Plasmas (Boca Raton, FL: CRC Press)
Rappazzo, A. F., Velli, M., Einaudi, G., & Dahlburg, R. B. 2005, ApJ, 633, 474
Roberts, D. A., Goldstein, M. L., Matthaeus, W. H., & Ghosh, S. 1992, JGR, 97, 17115
Rogers, M. M., & Moser, R. D. 1992, JFM, 243, 183

Samanta, T., Tian, H., Yurchyshyn, V., et al. 2019, Sci, 366, 890
Servidio, S., Matthaeus, W. H., & Dmitruk, P. 2008, PhRvL, 100, 095005
Shi, C., Velli, M., Tenerani, A., Rappazzo, F., & Réville, V. 2020, ApJ, 888, 68
Squire, J., Chandran, B. D. G., & Meyrand, R. 2020, ApJL, 891, L2
Tenerani, A., Velli, M., Matteini, L., et al. 2020, ApJS, 246, 32
Usmanov, A. V., Goldstein, M. L., & Matthaeus, W. H. 2014, ApJ, 788, 43
Usmanov, A. V., Goldstein, M. L., & Matthaeus, W. H. 2016, ApJ, 820, 17
Usmanov, A. V., Matthaeus, W. H., Goldstein, M. L., & Chhiber, R. 2018, ApJ, 865, 25
Verdini, A., Velli, M., Matthaeus, W. H., Oughton, S., & Dmitruk, P. 2010, ApJL, 708, L116
Yang, Y., Wan, M., Shi, Y., Yang, K., & Chen, S. 2016, JCoPh, 306, 73
Zank, G. P., Matthaeus, W. H., & Smith, C. W. 1996, JGR, 101, 17093